NACA

RESEARCH MEMORANDUM

for the

United States Air Force

LOW-SPEED WIND-TUNNEL INVESTIGATION OF THE DRAG OF A LOCKHEED F-94C AIRPLANE

(A.F. NO. 50-956)

By Ralph L. Maki

Ames Aeronautical Laboratory
Moffett Field, Calif.

NATIONAL ADVISORY COMMITTEE
FOR AERONAUTICS

WASHINGTON

April 25, 1952

NATIONAL ADVISORY COMMITTEE FOR AERONAUTICS

RESEARCH MEMORANDUM

for the

United States Air Force

LOW-SPEED WIND-TUNNEL INVESTIGATION OF THE DRAG OF A LOCKHEED F-94C AIRPLANE (A.F. NO. 50-956)

By Ralph L. Maki

SUMMARY

The aerodynamic characteristics in pitch of an F-94C airplane, with the primary attention given to its drag characteristics, have been evaluated at low speed in the Ames 40- by 80-foot wind tunnel. The increments of drag due to various surface irregularities, ports, and component parts of the production airplane were determined. Wing-wake surveys were taken to determine the section drag coefficients at midsemispan for the smooth and the production wing. Base-pressure and internal drags of the air-induction system were measured at low inlet-velocity ratios. The characteristics of the airplane in the landing configuration are also included.

INTRODUCTION

An investigation at low speeds of a Lockheed F-94C airplane has been made in the Ames 40- by 80-foot wind tunnel at the request of the U.S. Air Force. The study consisted of tests of the airplane in pitch with the primary purpose of assessing the increments of drag due to various surface irregularities, ports, and component parts of the airplane. Additional drag measurements consisted of momentum drag surveys at midsemispan and of internal and base-pressure drag surveys.

NOTATION

Coefficients and Dimensions

A	aspect ratio
b	wing span
c	wing chord, measured streamwise
$\bar{c}$	wing mean aerodynamic chord $\left(\frac{\int_0^{b/2} c^2 dy}{\int_0^{b/2} c\ dy}\right)$
C_D	drag coefficient
c_{d_o}	section drag coefficient
C_{D_P}	approximate parasite-drag coefficient $\left[C_D - \left(\frac{C_L^2}{\pi A}\right) \right]$
C_{D_T}	increment of drag coefficient due to wind-tunnel-wall interference
C_L	lift coefficient
C_l	rolling-moment coefficient
C_m	pitching-moment coefficient
C_{m_T}	increment of pitching-moment coefficient due to wind-tunnel-wall interference
C_n	yawing-moment coefficient
C_Y	side-force coefficient
d	tube spacing on wing-wake survey rake
F_c	wake-shape factor for compressible flow
F_i	wake-shape factor for incompressible flow

H	total pressure
n	number of active wing-wake survey-rake tubes
p	static pressure
q	dynamic pressure
R	wing Reynolds number $\left(\frac{V\bar{c}}{\nu}\right)$
R'	section Reynolds number $\left(\frac{Vc}{\nu}\right)$
S	area
s	wing-wake survey-rake height (nd)
V	velocity of air flow
w	wake width
y	spanwise distance from wing center line
α	free-stream angle of attack, referred to the fuselage center line
α_T	increment of angle of attack due to wind-tunnel-wall interference
η	fraction of semispan $\left(\frac{2y}{b}\right)$
ν	kinematic viscosity

Subscripts

o	free stream
W	wing
s_1	cooling-air exit
s_2	area of dead air between cooling-air duct and fuselage skin
e	cruise-jet exit

Wing-Wake and Duct-Survey Notation

Station locations indicated by subscripts as defined in figure 1.

Airplane Configurations

Wing study

W_1	wing completely smoothed and faired
W_2	wing surface in production condition aft of wing beam at 0.20c
W_3	W_2 with surface in production condition forward of wing beam
W_4	W_3 with surface in production condition on wing beam
W_5	W_4 with wing de-icing boots installed
W_6	W_5 with wing tanks pressurized at 6 pounds per square inch
a	ailerons deflected 2.5° up
T_1	wing tip tanks completely faired
T_2	standard wing tip tanks
δ	wing, trailing edge, split flaps deflected 45°

Fuselage study

B_1	fuselage completely faired, airspeed boom on, elliptical radome
B_2	B_1 with airspeed boom removed
B_3	B_2 with fuselage surface in production condition aft of wing trailing edge (faired covers on rear dive brakes removed)
B_4	B_2 with entire fuselage surface in production condition
B_5	B_4 with armament doors unsealed
B_6	B_5 with radar-cooler ports open

B_7 B_6 with gun-camera hole open

B_8 B_7 with hemispherical radome

B_9 B_7 with outer tail-fairing cone removed (cruise-jet fairing cone installed)

B_{10} B_9 with forward, fuselage, inlet, cooling-air holes open

B_{11} B_{10} with lowest pair of rear, fuselage, inlet, cooling-air holes open

B_{12} B_{10} with all rear, fuselage, inlet, cooling-air holes open

B_{13} B_{12} with cruise-jet fairing cone removed

B_{14} B_{13} with rear dive brakes open (dive-brake wells faired), fuselage tufted

B_{15} B_{13} with front dive brakes open, fuselage tufted

B_{16} B_{13} with all dive brakes open (rear dive-brake wells faired), fuselage tufted

B_{17} B_{16} with rear dive-brake-well fairings removed

E_1 large duct-inlet fairing removed (plug fairings installed)

E_2 E_1 with duct-inlet plug fairings removed

TEST AIRPLANE AND APPARATUS

A three-view sketch of the Lockheed F-94C test airplane (A.F. No. 50-956) is given in figure 2. Pertinent geometric data are listed in table I. The airplane was completely faired and smooth for the initial tests (configuration W_1B_1). All surface irregularities, ports, and access doors were smoothed and/or sealed. The air-induction system was closed with a smooth fairing over the duct inlets and a tail-cone fairing over the jet and cooling-shroud exits. A fairing on the rear fuselage lower surface enclosed the tail-support tip fittings for all the tests. A photograph of the airplane in configuration W_1B_1 is included as figure 3.

The changes in wing configuration are described in the Notation section from W_1 to W_6, together with T_1, T_2, a, and δ. Photographs (figs. 4 to 7) are included to show the major changes. Figure 4 shows the test airplane with the production wing and the smooth, faired fuselage (W_5B_2a). The detail photographs (figs. 5 and 6) show the de-icing boots installed and the ailerons deflected up 2.5° (W_5 and a). The wing fuel tanks were pressurized at 6 pounds per square inch for configuration W_6B_1a to duplicate any wing bulge present in normal flight conditions. The wing trailing-edge split flap is shown deflected 45° in figure 7.

The changes in fuselage configuration are described in the Notation section from B_1 to B_8 and B_{14} to B_{17}. Some of the major changes are shown in figures 3, 4, and 8 to 10. Figures 3 and 4 show the airplane with the airspeed boom on (B_1) and off (B_2). Views with the dive brakes extended are given in figure 8. A comparison of the rear dive-brake covers faired and unfaired can be seen in figures 9 and 10, respectively. The armament doors (B_5) are large access doors on the fuselage upper surface forward of the canopy. The radar cooler inlet (B_6) is visible in figure 4 just behind the radome on the fuselage upper surface.

Alterations to the air-induction system are described by configurations B_9 to B_{13}, E_1 and E_2. The photographs of figures 3, 4, and 9 to 13 show the changes. The fairing over the duct inlet can be seen in figures 3 and 4. Figures 9 to 11 show the progressive opening of the duct outlets described by notations B_7, B_9, and B_{13}. Duct-inlet changes E_1 and E_2 are pictured in figures 12 and 13. For these studies the engine remained installed in the airplane and was locked to prevent it from windmilling when the duct inlets and outlets were open.

Figure 14 shows the airplane in configuration $W_5B_{13}E_2a\delta$ (except that the plug fairing of the left duct inlet is installed) which represents the production airplane with the flaps lowered as used for landing approaches.

Details of the survey rake used to measure wing section drag by the momentum-loss method are shown in figure 15. The structure used to support the rake behind the wing trailing edge was mounted on the floor of the wind tunnel and was independent of the tunnel-scale system. Details of the duct survey rakes are given in figure 16. In figure 11, these rakes can be seen partially installed.

CORRECTIONS

The measured angles of attack and drag coefficients have been corrected for stream-angle inclination. Corrections for wind-tunnel-wall interference were applied as follows:

$$\alpha_T = 0.49\ C_L$$

$$C_{D_T} = 0.0085\ C_L^2$$

$$C_{m_T} = 0.012\ C_L$$

These corrections were added to the measured results.

Drag and pitching-moment tares based on tests of a rectangular wing of comparable size were applied to the data. To account approximately for the different support-strut arrangement used in these tests, the drag and pitching moments of the support struts with the tunnel empty were measured. These measured values were used as the total zero-lift tares, and the usual tare curves were shifted to pass through these zero-lift points. The tares subtracted from the data were as follows:

C_L	-0.2	0	0.4	0.8	1.2
$C_{D_{tare}}$	0.0058	0.0050	0.0034	0.0018	0.0005
$C_{m_{tare}}$	-.0106	-.0119	-.0147	-.0174	-.0201

All tests in which base-pressure or internal-drag surveys were made had a bundle of pressure tubes exposed on the rear support-strut tip (fig. 11) which added to the measured airplane drag and altered the airplane pitching moments. Configuration $W_5B_{13}E_1a$ was tested with the tubing present and removed to establish the values of the tares due to the presence of the tubing. These tares have been applied to the drag and pitching moments of all configurations which had the tubing present.

The tares subtracted from the data were:

$$C_{D_{tare}} = 0.0011 + 0.0002\ C_L$$

$$C_{m_{tare}} = -0.0066$$

The effect of the tubing on the measured lift was small and has been neglected.

TESTS AND RESULTS

The test results are presented in figures 17 to 36. Table II is an index to the figures. The majority of the tests were made at a free-stream dynamic pressure of about 70 pounds per square foot, with some tests ranging from about 20 to 130 pounds per square foot. The Mach number range was from 0.11 to 0.30, and the Reynolds number range was from 5.4×10^6 to 13.2×10^6 based on $\bar{c}$. For all the tests the rudder, elevators, and stabilizer remained undeflected, and the airplane was at 0° sideslip. Deflections of the ailerons and flaps are specified in the figures by the notations a and δ (defined in the Notation section). Measurements of lift, drag, and pitching moment were made on all test configurations, including those for which wing-wake and duct exit surveys were taken.

The results of the wing studies are presented in figures 17 to 26. The force data showing the effects of wing tip tanks and the progressive removal of wing fairings are given in figures 17 to 22. Results of the wing-wake surveys at midsemispan, together with force data recorded while the surveys were being made, are given in figures 23 to 26. The wake surveys were taken at a point 10.2-percent chord aft of the wing trailing edge at 0.489 semispan. The wing chord at this semispan station was taken to be 76.65 inches. Section drag coefficients were determined from the measured static and total pressures in the wing wake by the expression given in reference 1,

$$c_{d_o} = \frac{F_c}{F_i}\left[F_i\,\frac{w}{\bar{c}}\,\frac{(H_o-H_1)_{av}}{(H_o-p_o)}\right]$$

The results of the fuselage studies are presented in figures 27 to 31. The data in figure 29 show the effects of variation of Reynolds number on the airplane with the wing and fuselage in production condition, but with the tail-cone fairing and the duct-inlet fairing on. These

fairings were not installed and the main duct inlet was open for the tests showing the effects of opening the dive brakes (figs. 30 and 31). As will be discussed later, the significance of these results is questionable.

The results of the air-induction-system studies are presented in figures 32 to 34. The base-pressure and internal-drag-survey results given in figure 32 are separated into the drags measured over the cooling-air outlet (S_{s_1}), over the jet-exit nozzle (S_e), and over the area of dead air between the cooling-air periphery and the fuselage skin (S_{s_2}). The base-pressure drag coefficients were determined by the measured decrement in static pressure from the free-stream value to that at the duct outlets by the expression

$$C_{D_{\text{base pressure}}} = \frac{S_4 (p_o - p_4)}{q_o S_W}$$

The internal drag coefficients also were referenced to free-stream conditions, and were computed from the expression

$$C_{D_{\text{internal}}} = 2 \frac{S_4}{S_W} \sqrt{1 - \left(\frac{H_o - H_4}{q_o}\right) - \left(\frac{p_4 - p_o}{q_o}\right)} \left[1 - \sqrt{1 - \left(\frac{H_o - H_4}{q_o}\right)}\right]$$

This expression was derived directly from the basic momentum-loss expression, $D_{\text{internal}} = m(V_o - V_5)$, with the following assumptions:

$$H_1 = H_o$$

$$H_4 = H_5$$

$$p_5 = p_o$$

Estimates of the flow velocities through the ducting with inlets and outlets open indicated inlet-velocity ratios of about 0.3 for both the main and the cooling-air jets. The low flow velocity through the main duct is attributed to the presence of the engine, locked to prevent its windmilling. The unavoidably low flow velocities in the ducts were not representative of flight conditions and also may have affected the external flow conditions. Therefore, the measured internal drags must be considered inapplicable for comparison with flight conditions, and the measured force characteristics of all configurations with the cooling-air and main duct inlets open (notations E_1 and E_2) are of dubious value.

The characteristics of the test airplane in landing condition were determined to angles of attack beyond the stall (fig. 35). The Reynolds number for this test, 7.8×10^6, is approximately equal to the landing Reynolds number of the airplane.

Figure 36 is presented as a summarization of the minimum drags of the configurations tested. The increments of drag contributed by wing and fuselage irregularities and roughness were small. In view of the low flow velocities through the ducts, the test results on configurations with flow through the ducts are of questionable significance.

Ames Aeronautical Laboratory
National Advisory Committee for Aeronautics
Moffett Field, Calif.

REFERENCE

1. Davis, Wallace F.: Comparison of Various Methods for Computing Drag from Wake Surveys. NACA ARR, 1943

TABLE I. - GEOMETRIC DATA ON THE LOCKHEED F-94C AIRPLANE

Wing	
Area, square feet	232.81
Span, feet	37.26
Aspect ratio	5.96
Taper ratio	0.38
Dihedral angle, degrees	8
Mean aerodynamic chord, feet	6.72
Sweepback of the 52-percent chord line, degrees	0
Incidence of the root chord, degrees	2.0
Incidence of the tip chord, degrees	-1.5
Airfoil section, streamwise	NACA 64A210
Trailing-edge split flap (data for one side only)	
Span, feet	8.52
Hinge line, percent chord	75
Deflection, degrees	45
Fuselage	
Over-all length, feet	41.42
Maximum width, feet	4.67
Fineness ratio	8.9

TABLE II. - SUMMARY OF CONFIGURATIONS TESTED

Phase of study	Figure number	Configuration	Reynolds number	Data presented
Wing	17	W_1B_1 with wing tips faired	Variable	C_L vs C_D, α, C_m
	18	W_1B_1 and W_1B_1 with wing tips faired	10.3×10^6	
	19	$W_1B_1T_2$	Variable	
	20	W_1B_1, $W_1B_1T_2$, and $W_1B_1T_1$	10.3×10^6	
	21	$W_{1-5}B_1$, W_5B_1a, and W_6B_1a		
	22			C_{D_P} vs C_L
	23	W_1B_1	Variable	c_{d_o} vs C_T
	24			C_L vs C_D, α, C_m
	25	W_6B_1a		c_{d_o} vs C_L
	26			C_L vs C_D, α, C_m
Fuselage	27	$W_5B_{2-8}a$	10.3×10^6	
	28			C_{D_P} vs C_L
	29	W_5B_7a	Variable	C_L vs C_D, α, C_m
Dive brakes	30	$W_5B_{14-17}E_2a$	10.3×10^6	
	31			C_{D_P} vs C_L
Ducting	32	$W_5B_{9-12}a$,		C_D vs C_L
	33	$W_5B_{12-13}E_1a$, and		C_L vs C_D, α, C_m
	34	$W_5B_{13}E_2a$		C_{D_P} vs C_L
Landing condition	35	$W_5B_{13}E_2a\delta$	7.8×10^6	C_L vs C_D, α, C_m, C_Y, C_n, C_l
Summary	36	Several	10.3×10^6	$C_{D_{min}}$ vs configuration

FIGURE LEGENDS

Figure 1.- Notation for wing-wake and duct survey measurements. (a) Wing wake-survey notation. (b) Duct-survey notation.

Figure 2.- Three-view sketch of the test airplane.

Figure 3.- View of the airplane mounted in the wind tunnel. Configuration W_1B_1.

Figure 4.- General view of the test airplane. Configuration W_5B_2a.

Figure 5.- View of the right-wing panel showing the de-icing boot installed.

Figure 6.- View from below of the right-wing panel showing the details of the de-icing boot and the aileron deflected up 2.5°.

Figure 7.- View from below of the right-wing panel showing the split flap deflected 45°.

Figure 8.- View from below with the dive brakes extended. Configuration $W_5B_{16}E_2a$ without tufts. (a) View looking rearward.

Figure 8.- Concluded. (b) View looking forward.

Figure 9.- View of the rear fuselage area of the test airplane showing the large tail-cone fairing and the faired covers on the rear dive brakes.

Figure 10.- View of the rear fuselage area of the test airplane showing the cruise-jet tail-cone fairing and the standard rear dive-brake covers. Portions of the cooling-shroud-rake installations are visible.

Figure 11.- View of the rear fuselage area of the test airplane showing the rakes being installed in the cruise-jet exit.

Figure 12.- View from below of the duct inlets with plug fairings installed.

Figure 13.- View from below of the duct inlets with the plug fairing removed from the right duct inlet.

Figure 14.- General view of the test airplane with flaps deflected 45°. Configuration $W_5B_{13}a\delta$ and the right duct inlet as E_2.

Figure 15.- Details of the wing-wake-survey rake.

Figure 16.- Details of the duct-survey rakes.

Figure 17.- Aerodynamic characteristics of the test airplane. Configuration W_1B_1 with the wing tips faired, at two Reynolds numbers.

Figure 18.- Aerodynamic characteristics of the test airplane. Configurations W_1B_1 and W_1B_1 with the wing tips faired. R, 10.2×10^6.

Figure 19.- Aerodynamic characteristics of the test airplane. Configuration $W_1B_1T_2$, at two Reynolds numbers.

Figure 20.- Aerodynamic characteristics of the test airplane with and without standard and faired wing tip tanks. R, 10.3×10^6.

Figure 21.- Effects of several wing changes on the aerodynamic characteristics of the test airplane. R, 10.3×10^6. (a) C_L vs C_D.

Figure 21.- Continued. (b) C_L vs α.

Figure 21.- Concluded. (c) C_L vs C_m.

Figure 22.- Effects of several wing changes on parasite drag of the test airplane. R, 10.3×10^6.

Figure 23.- Wing section drag coefficient at .489 semispan at several Reynolds numbers. Airplane configuration W_1B_1.

Figure 24.- Aerodynamic characteristics of the test airplane. Configuration W_1B_1, at several Reynolds numbers. (a) C_L vs C_D.

Figure 24.- Continued. (b) C_L vs α.

Figure 24.- Concluded. (c) C_L vs C_m.

Figure 25.- Wing section drag coefficient at .489 semispan at several Reynolds numbers. Airplane configuration W_6B_1a.

Figure 26.- Aerodynamic characteristics of the test airplane. Configuration W_6B_1a, at several Reynolds numbers. (a) C_L vs C_D.

Figure 26.- Continued. (b) C_L vs α.

Figure 26.- Concluded. (c) C_L vs C_m.

Figure 27.- Effects of several fuselage changes on the aerodynamic characteristics of the test airplane. R, 10.3×10^6. (a) C_L vs C_D.

Figure 27.- Continued. (b) C_L vs α.

Figure 27.- Concluded. (c) C_L vs C_m.

Figure 28.- Effects of several fuselage changes on the parasite drag of the test airplane. R, 10.3×10^6.

Figure 29.- Aerodynamic characteristics of the test airplane. Configuration W_5B_7a, at several Reynolds numbers.

Figure 30.- Effects of opening the dive brakes on the aerodynamic characteristics of the test airplane. R, 10.3×10^6.

Figure 31. Effects of opening the dive brakes on the parasite drag of the test airplane. R, 10.3×10^6.

Figure 32.- Increments of airplane drag coefficient due to base-pressure drag and due to cooling-air and main duct internal drags. R, 10.3×10^6. (a) Cooling-air duct drags.

Figure 32.- Concluded. (b) Main duct drags.

Figure 33.- Effects of opening the duct outlets and inlets on the aerodynamic characteristics of the test airplane. R, 10.3×10^6. (a) C_L vs C_D.

Figure 33.- Continued. (b) C_L vs α.

Figure 33.- Concluded. (c) C_L vs C_m.

Figure 34.- Effects of opening the duct outlets and inlets on the parasite drag of the test airplane. R, 10.3×10^6.

Figure 35.- Aerodynamic characteristics of the test airplane. Configuration $W_5B_{13}E_{2ao}$ R, 7.8×10^6. (a) C_L vs C_D, α, C_m.

Figure 35.- Concluded. (b) C_L vs C_Y, C_n, C_l.

Figure 36.- Summary of the minimum drag coefficients at a Reynolds number of 10.3×10^6.

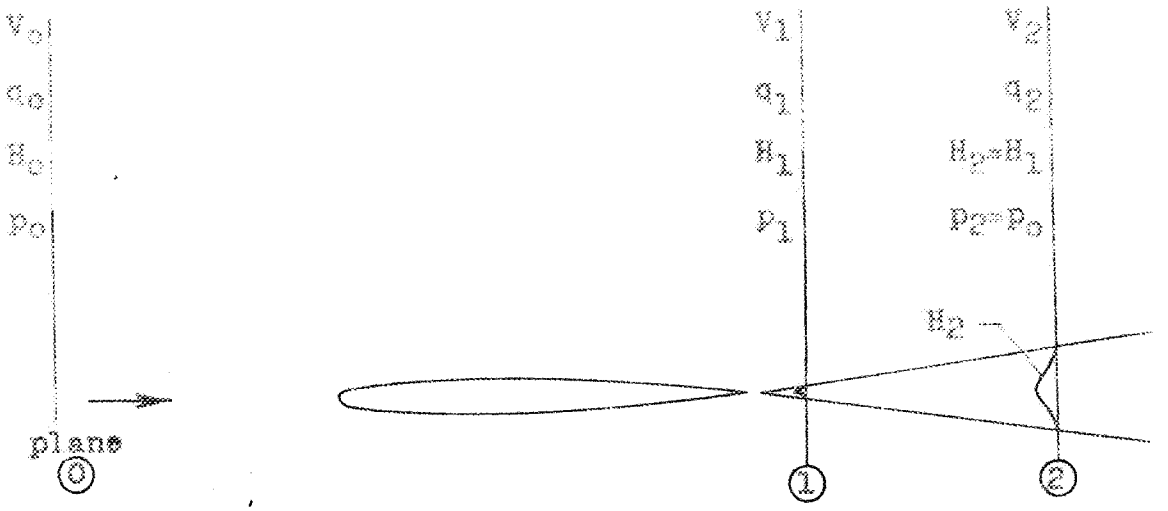

(a) Wing wake-survey notation.

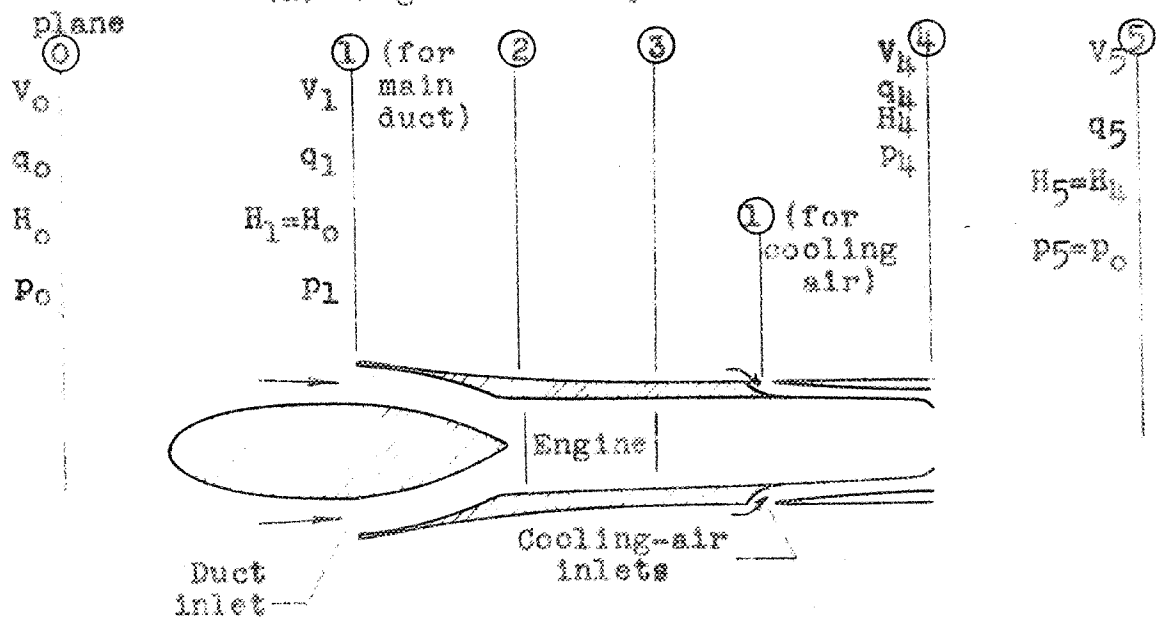

(b) Duct-survey notation.

Figure 1.- Notation for wing-wake and duct survey measurements.

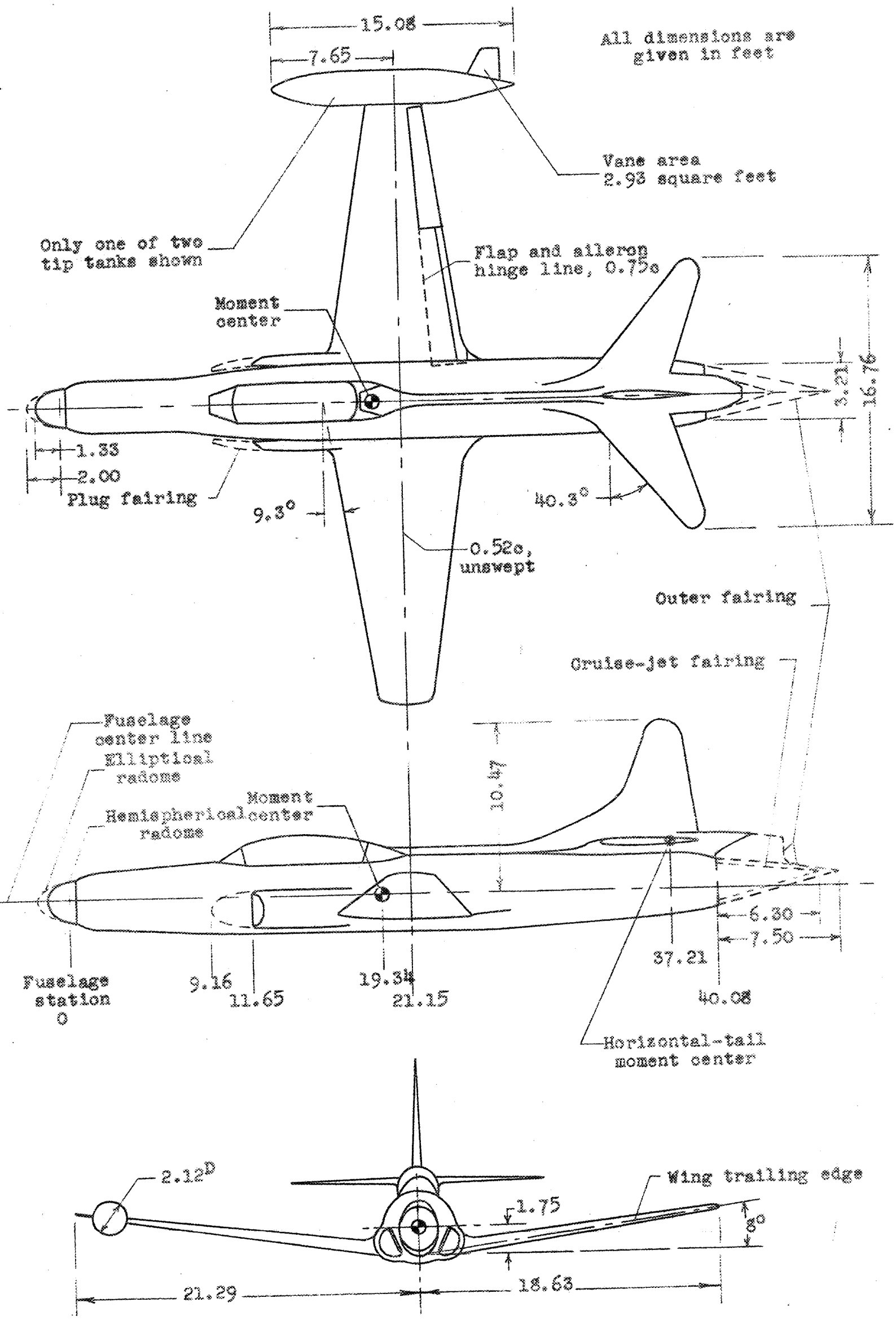

Figure 2.- Three-view sketch of the test airplane.

Figure 3.- View of the airplane mounted in the wind tunnel. Configuration W_1B_1.

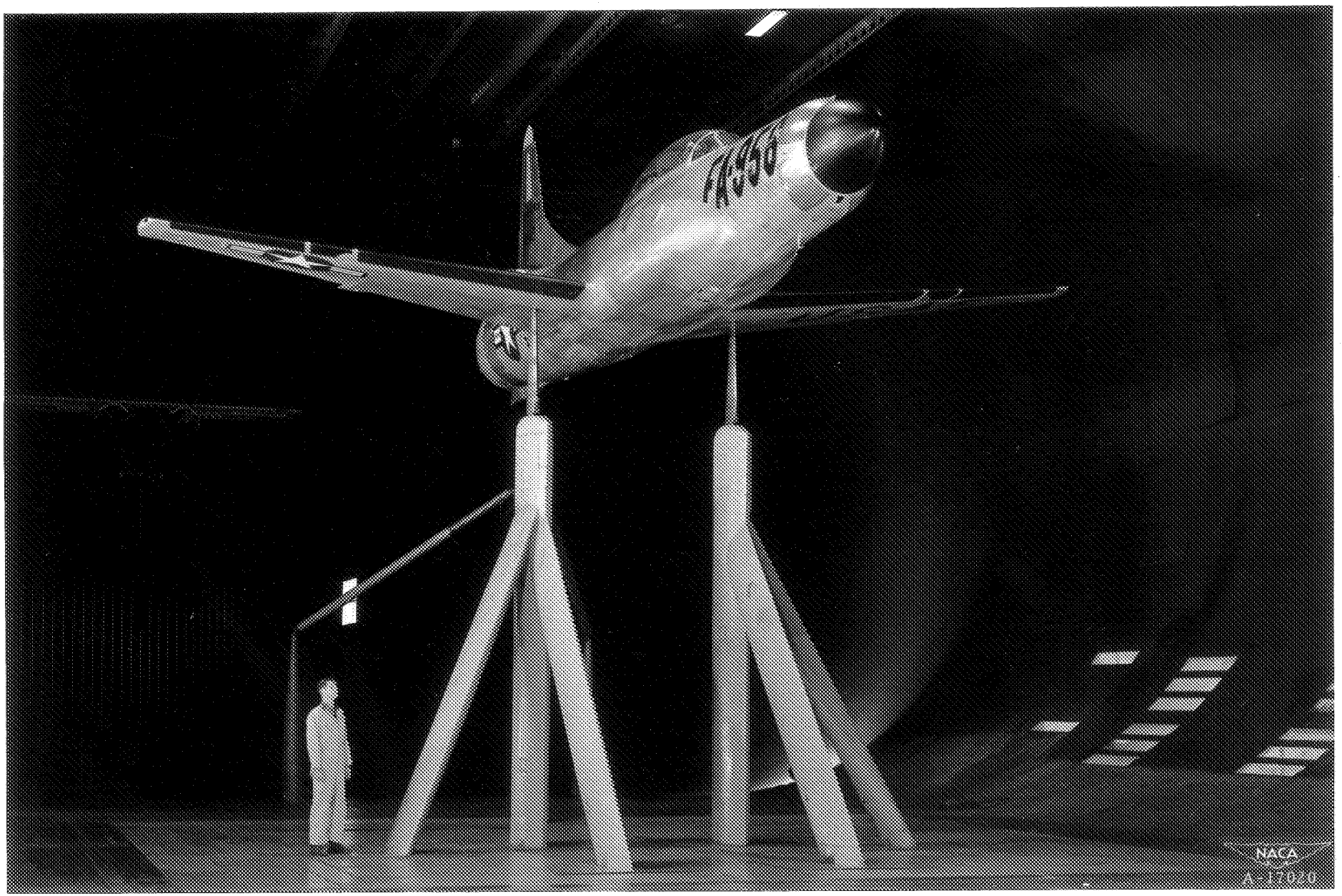

Figure 4.- General view of the test airplane. Configuration W_5B_2a.

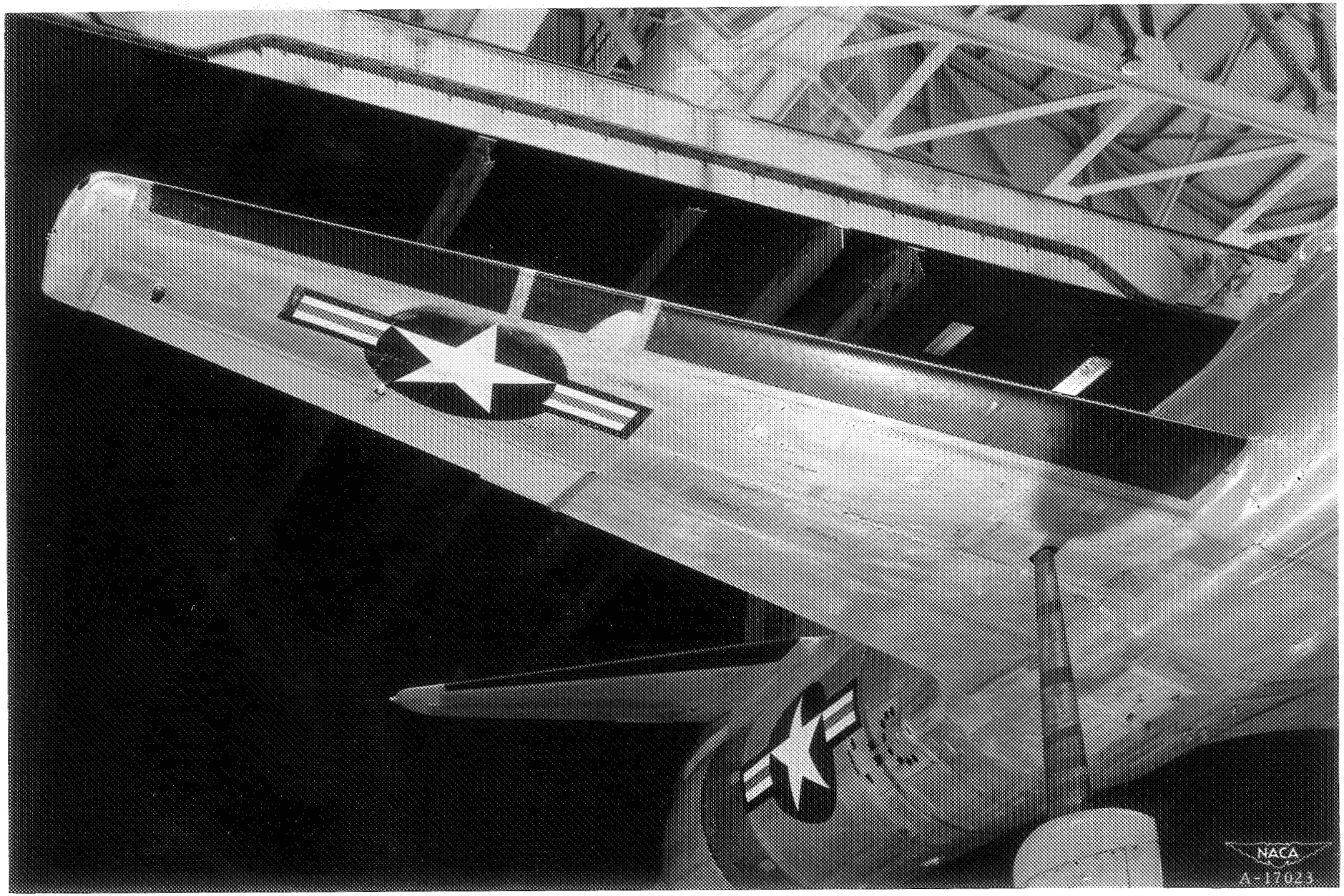

Figure 5.- View of the right wing panel showing the de-icing boot installed.

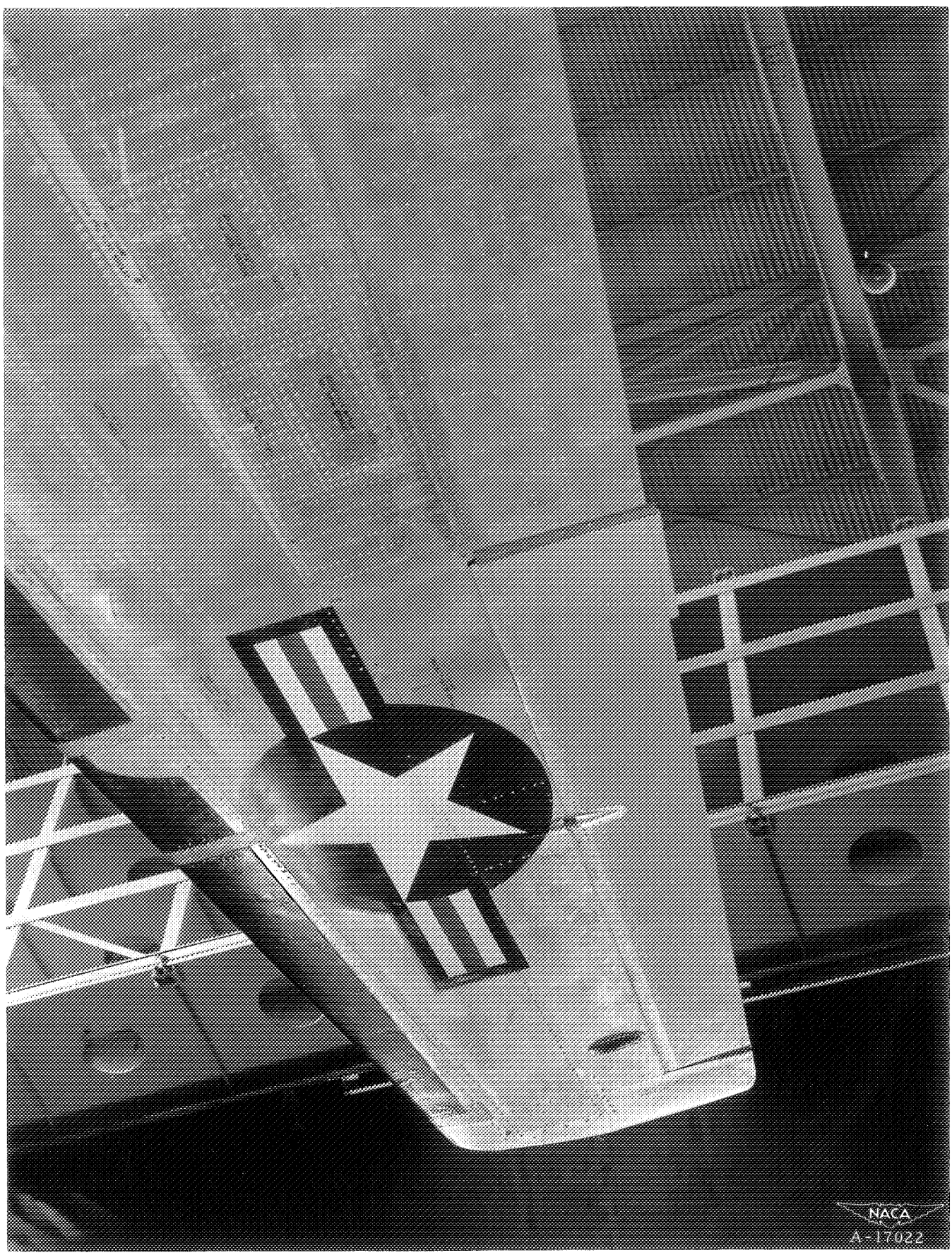

Figure 6.- View from below of the right wing panel showing the details of the de-icing boot and the aileron deflected up 2.5°.

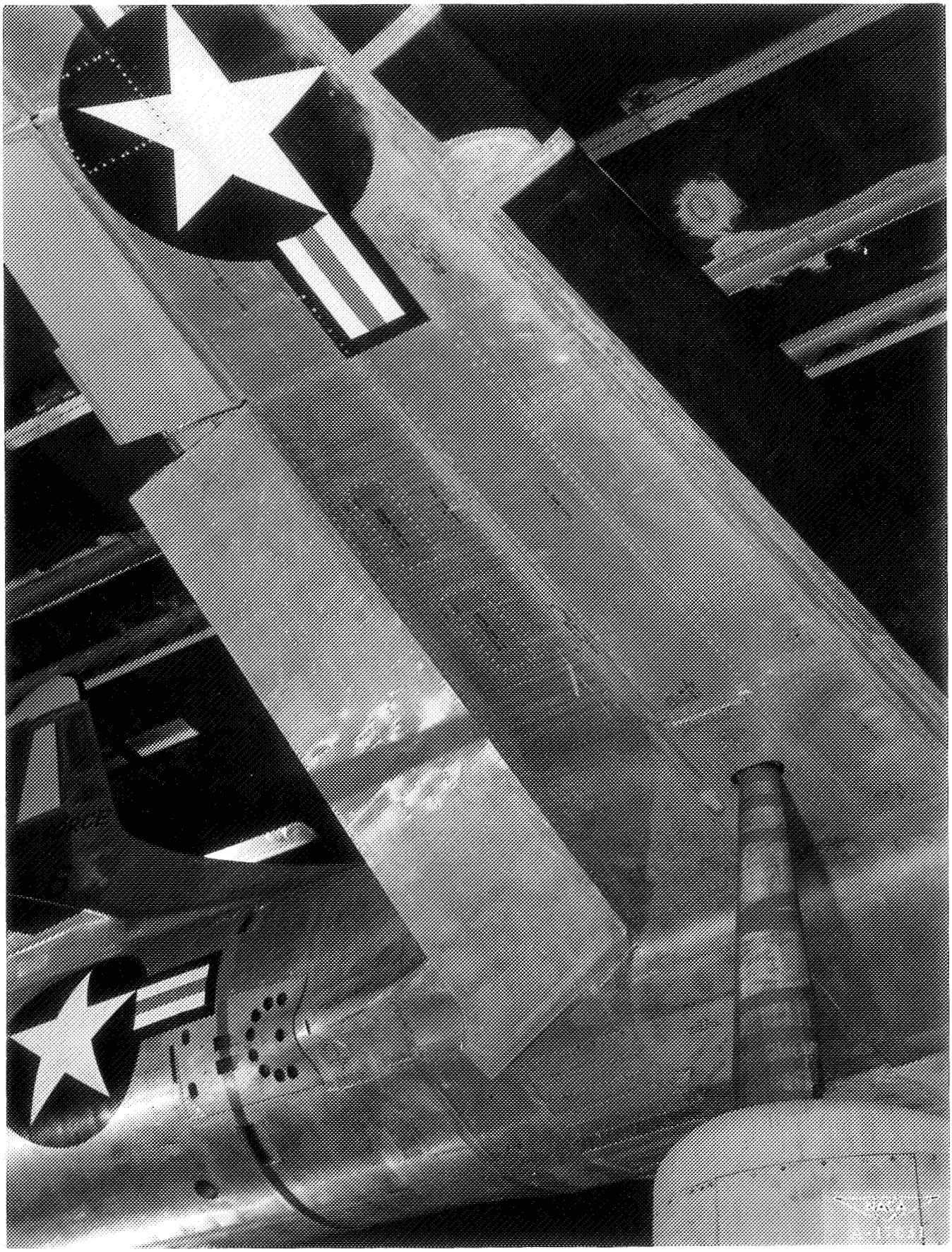

Figure 7.- View from below of the right wing panel showing the split flap deflected 45°.

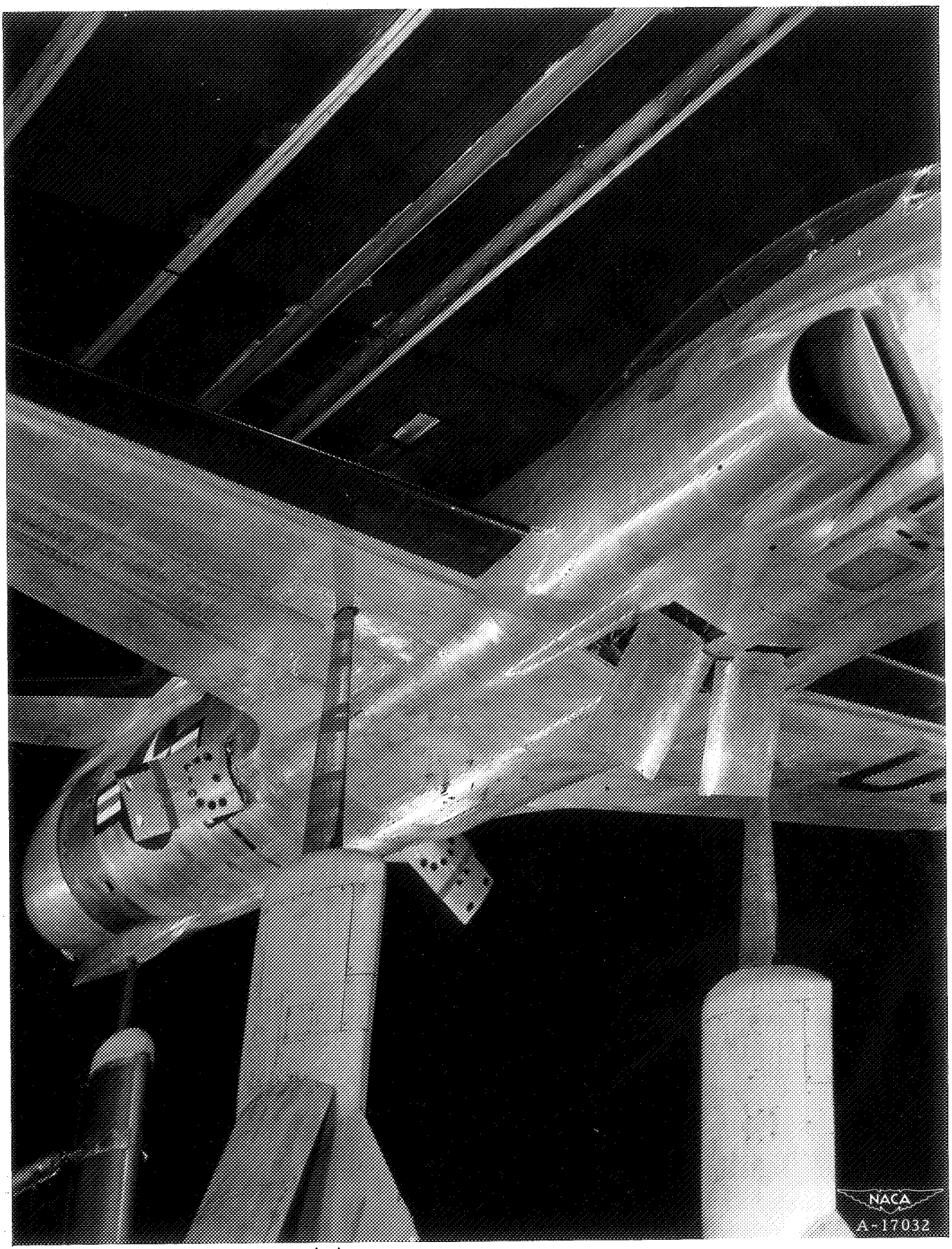

(a) View looking rearward.

Figure 8.- View from below with the dive brakes extended. Configuration $W_5B_{16}E_2a$, without tufts.

(b) View looking forward.

Figure 8.- Concluded.

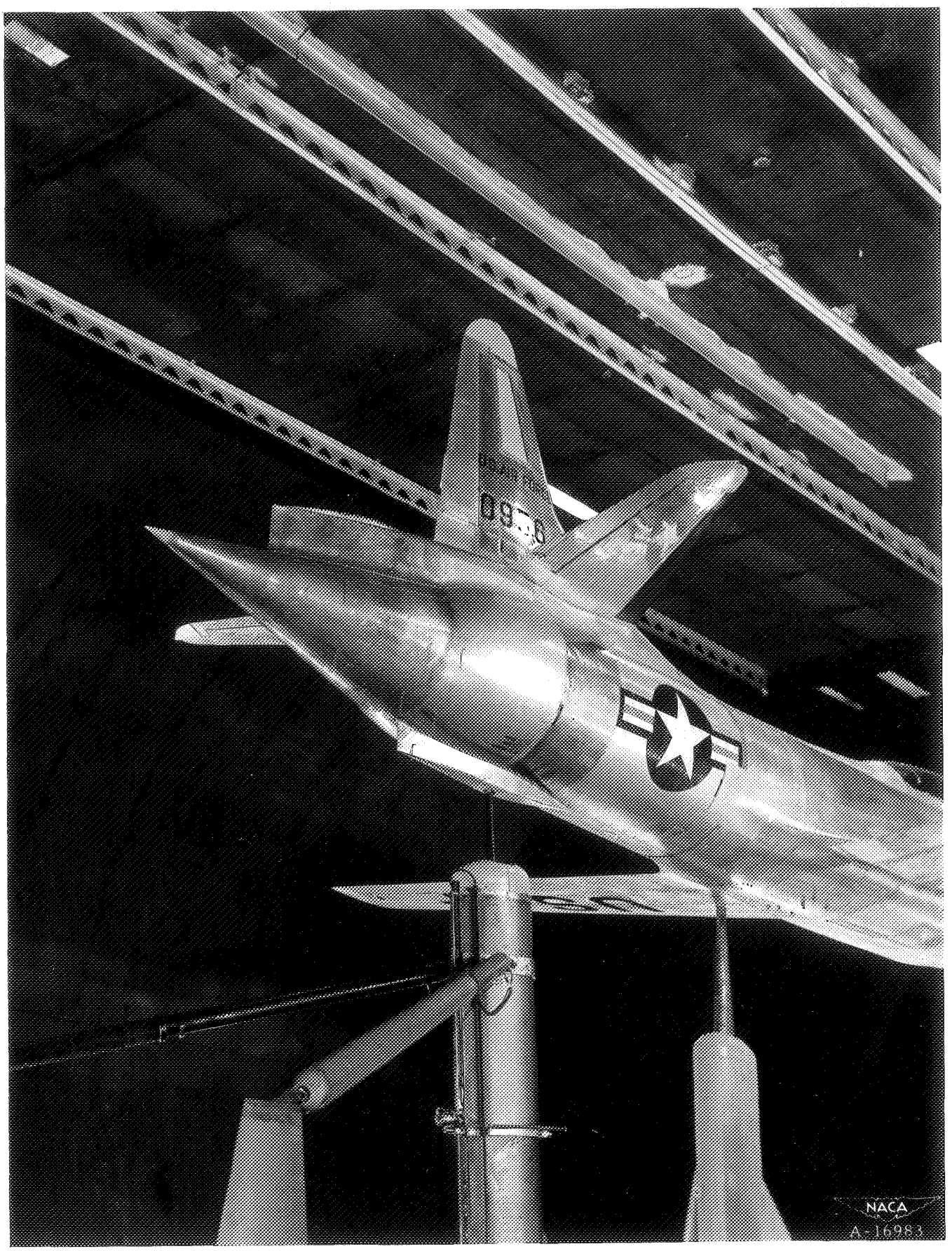

Figure 9.- View of the rear fuselage area of the test airplane showing the large tail-cone fairing and the faired covers on the rear dive brakes.

Figure 10.- View of the rear fuselage area of the test airplane showing the cruise-jet tail-cone fairing and the standard rear dive-brake covers. Portions of the cooling-shroud-rake installations are visible.

Figure 11.- View of the rear fuselage area of the test airplane showing the rakes being installed in the cruise-jet exit.

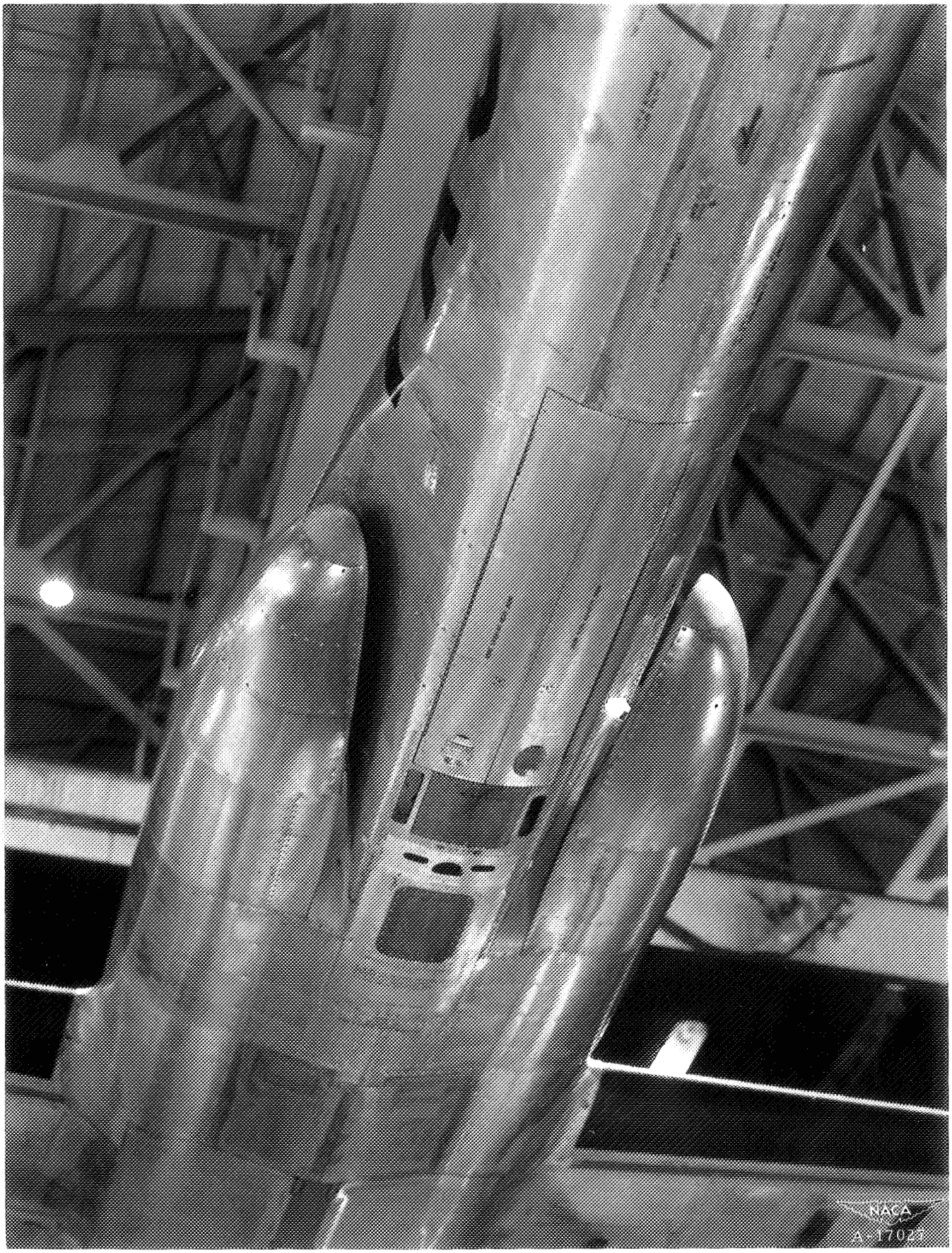

Figure 12.- View from below of the duct inlets with plug fairings installed.

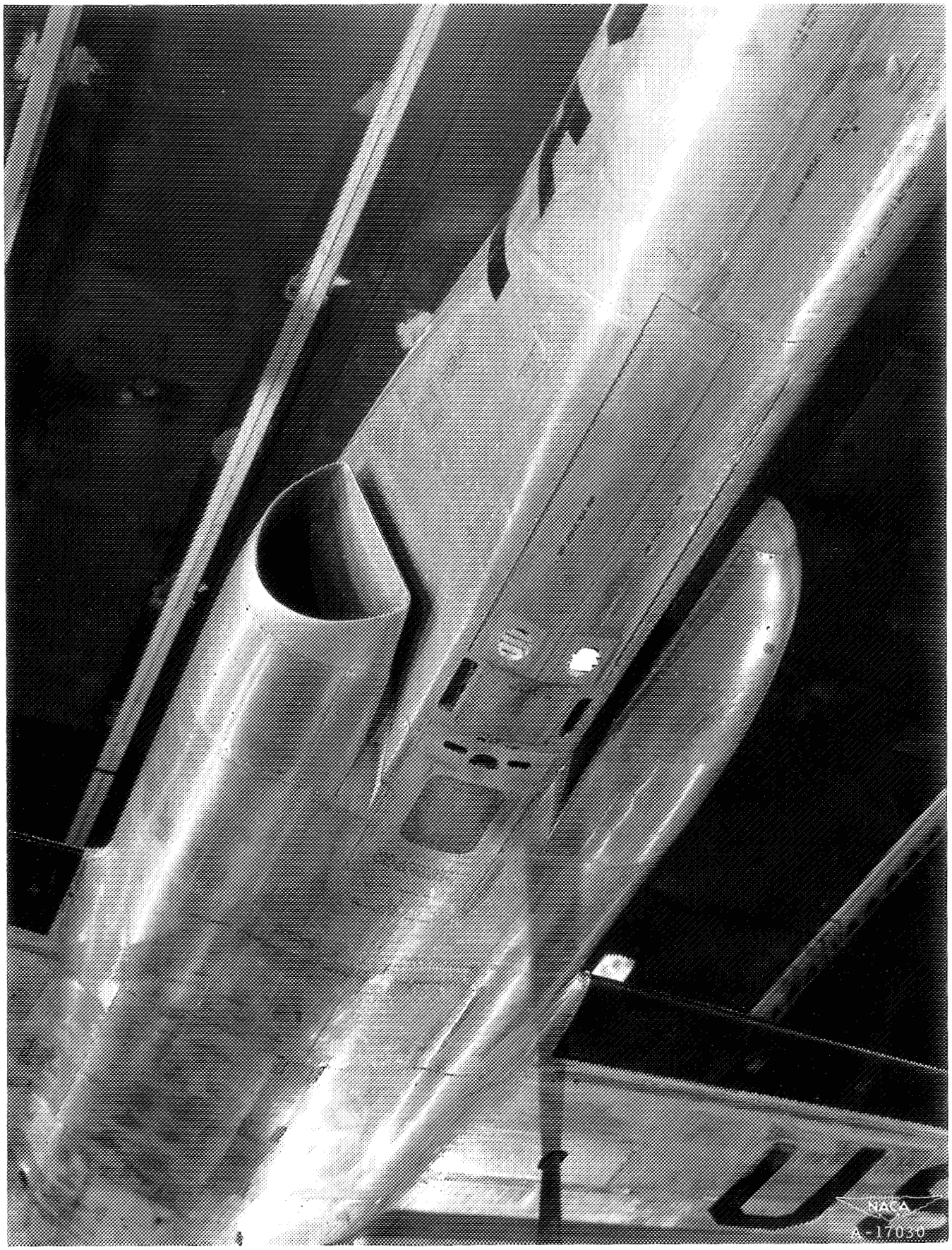

Figure 13.- View from below of the duct inlets with the plug fairing removed from the right duct inlet.

Figure 14.- General view of the test airplane with flaps deflected 45°. Configuration $W_5B_{13}a\delta$ and the right duct inlet as E_2.

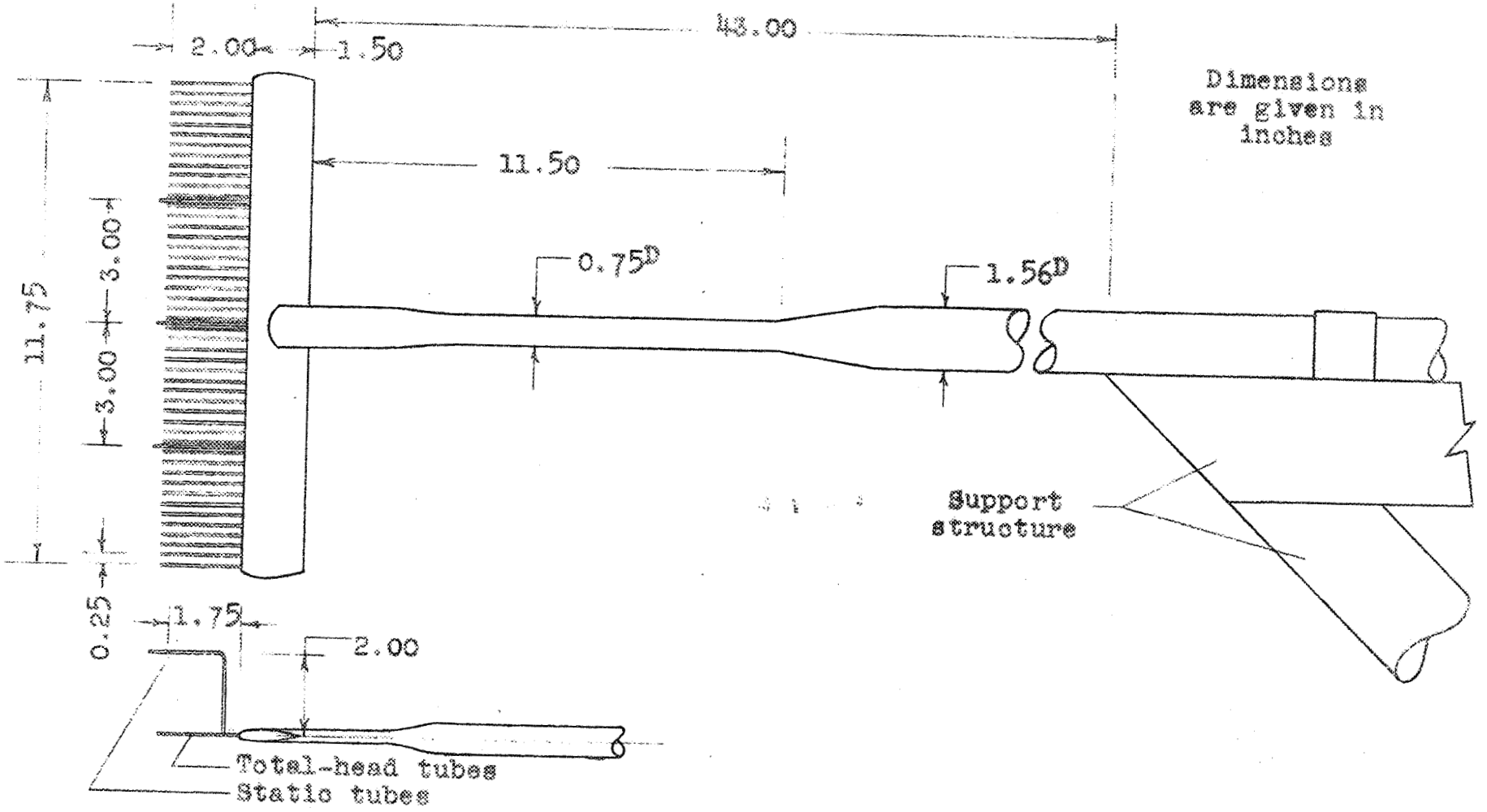

Figure 15.- Details of the wing-wake-survey rake.

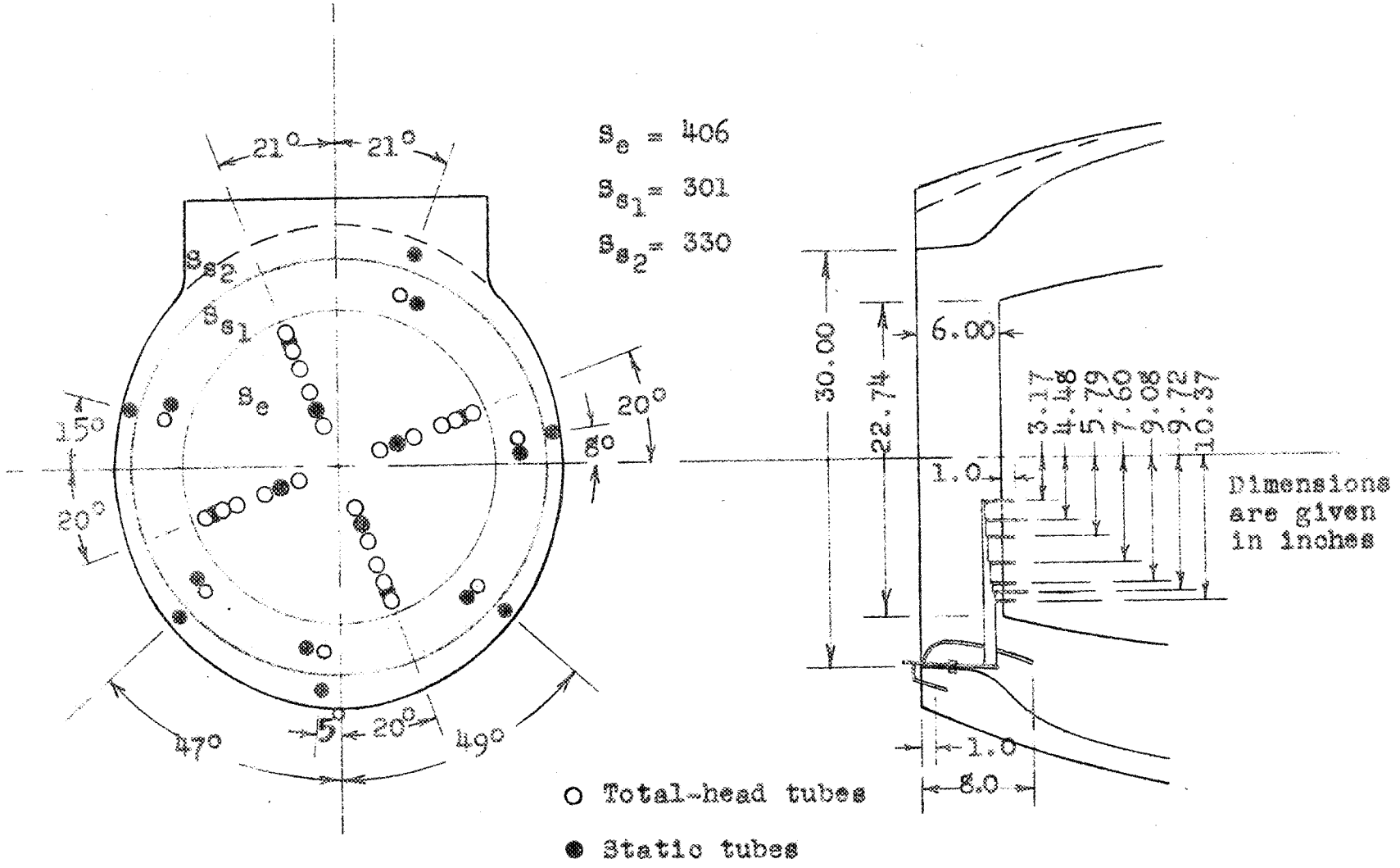

Figure 16.- Details of the duct-survey rakes.

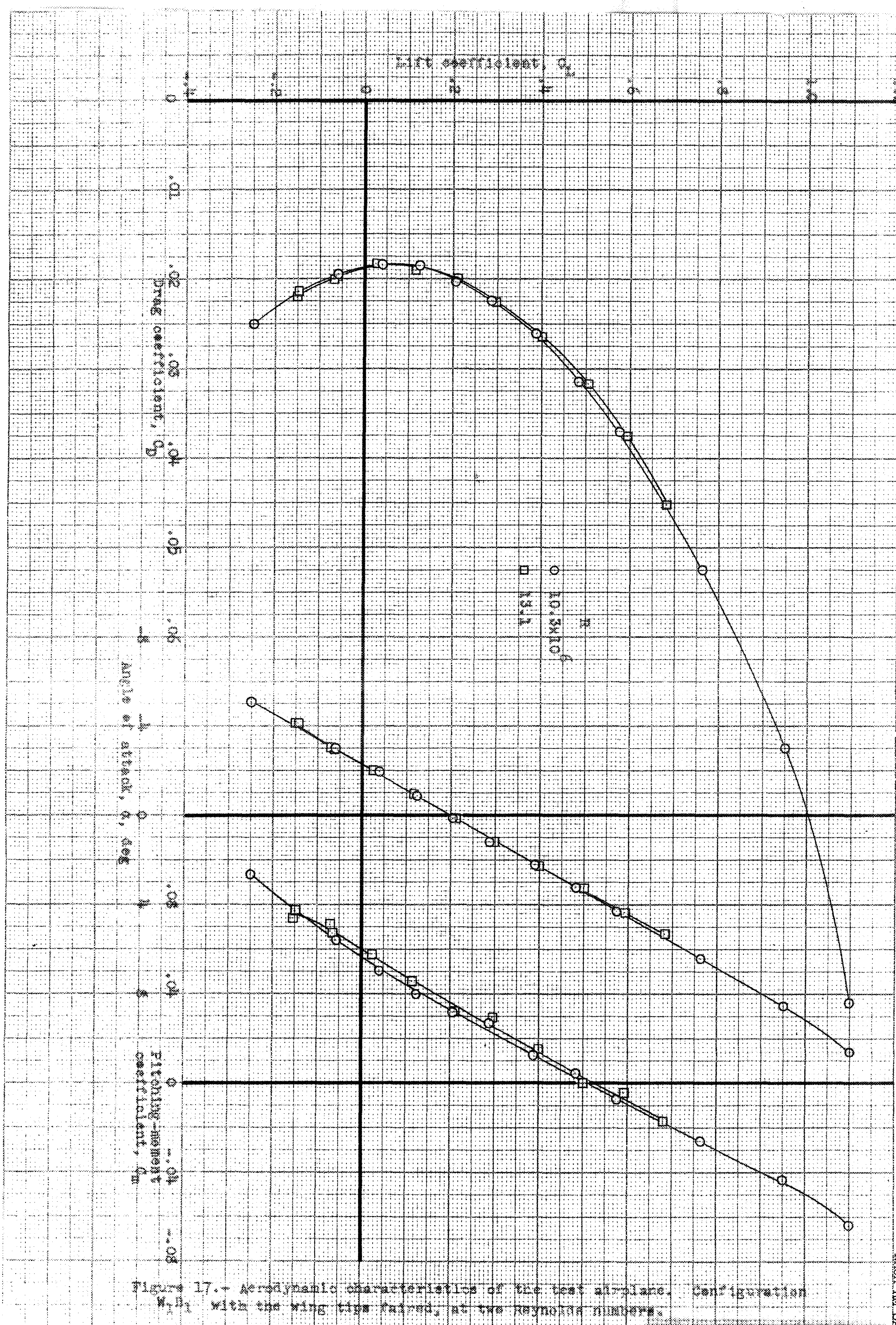

Figure 17.- Aerodynamic characteristics of the test airplane. Configuration W_1B_1 with the wing tips faired, at two Reynolds numbers.

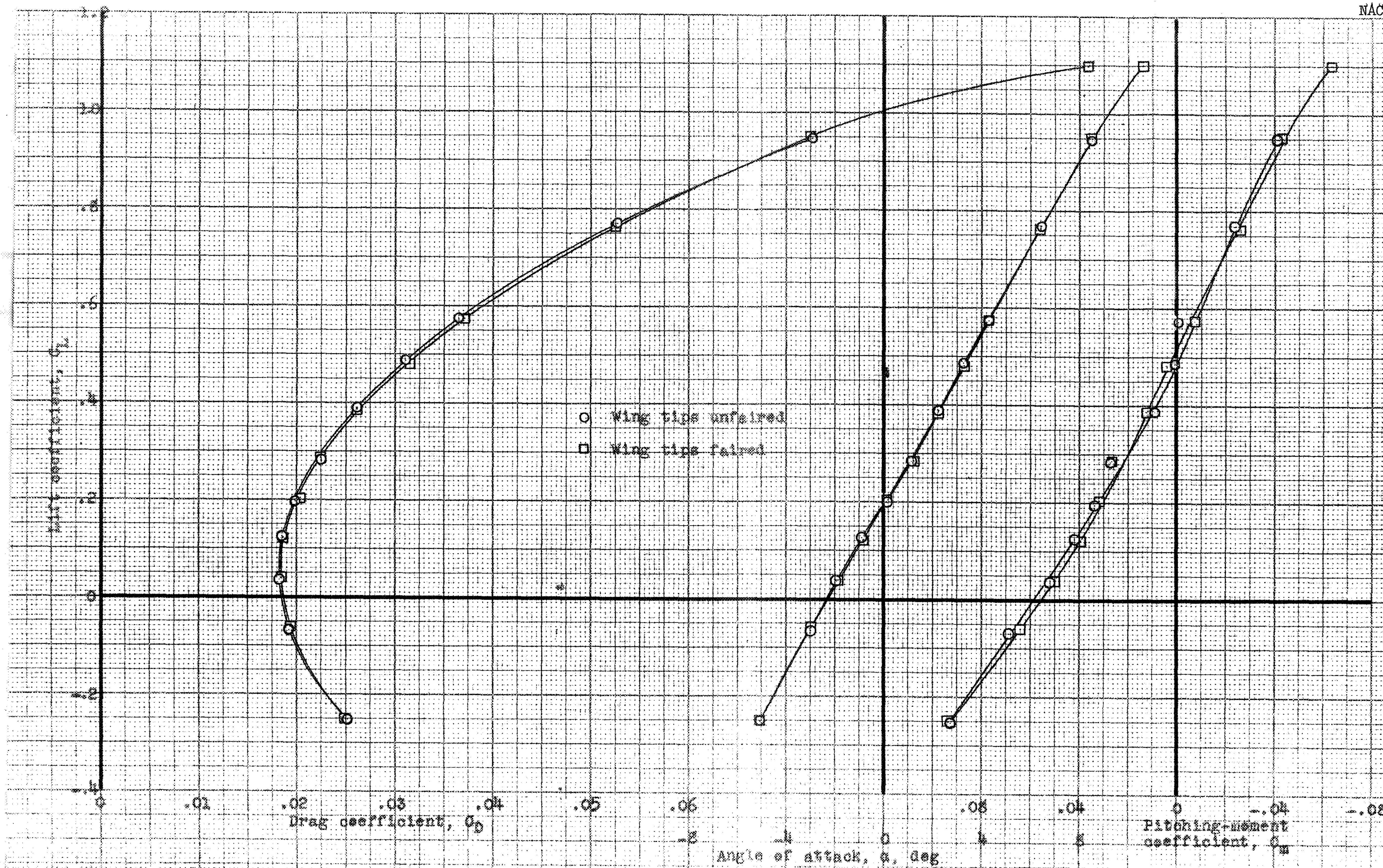

Figure 18.- Aerodynamic characteristics of the test airplane, configurations W_1B_1, and W_1B_1 with the wing tips faired. R, 11.3×10[6].

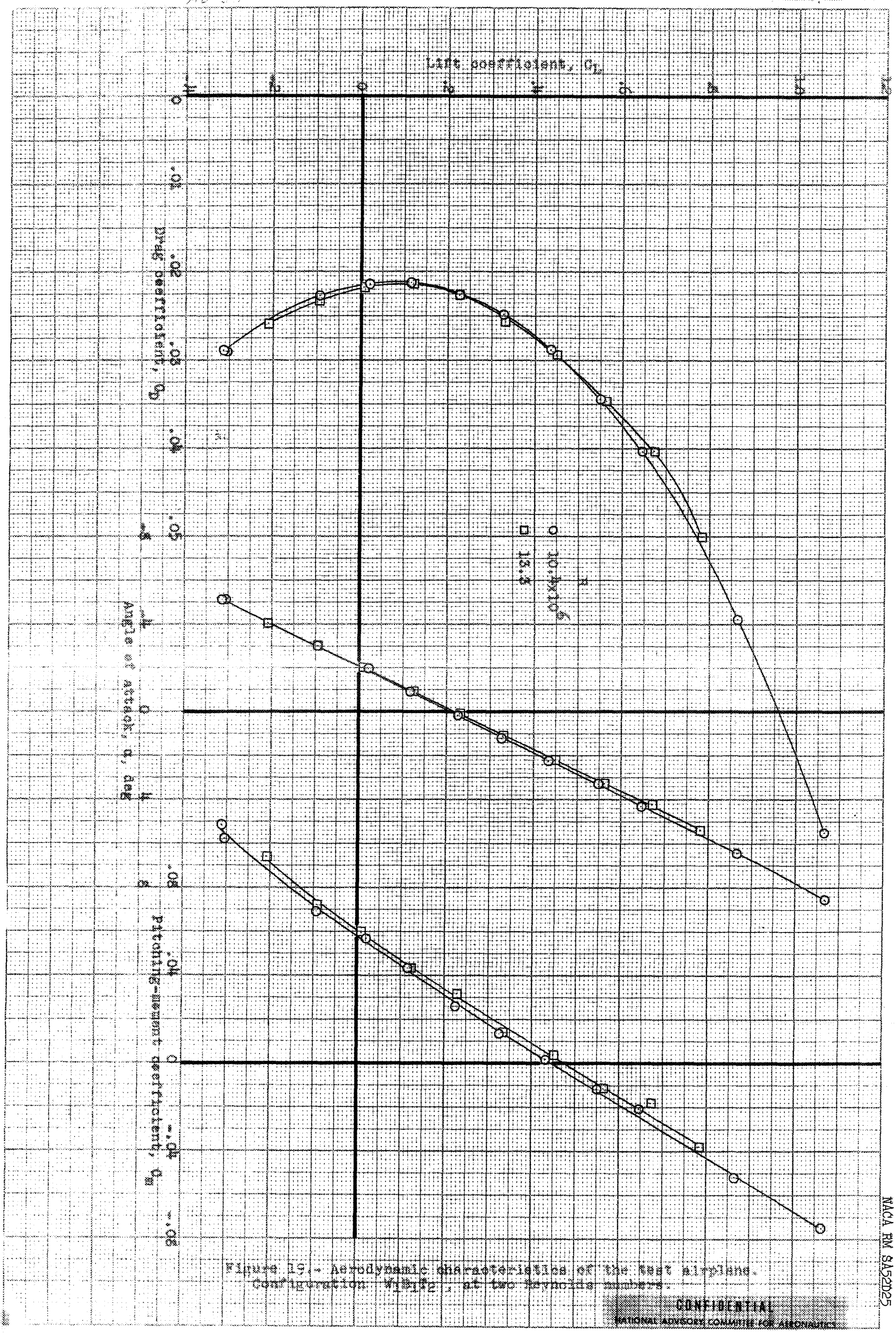

Figure 19.- Aerodynamic characteristics of the test airplane. Configuration: Wing-fin, at two Reynolds numbers.

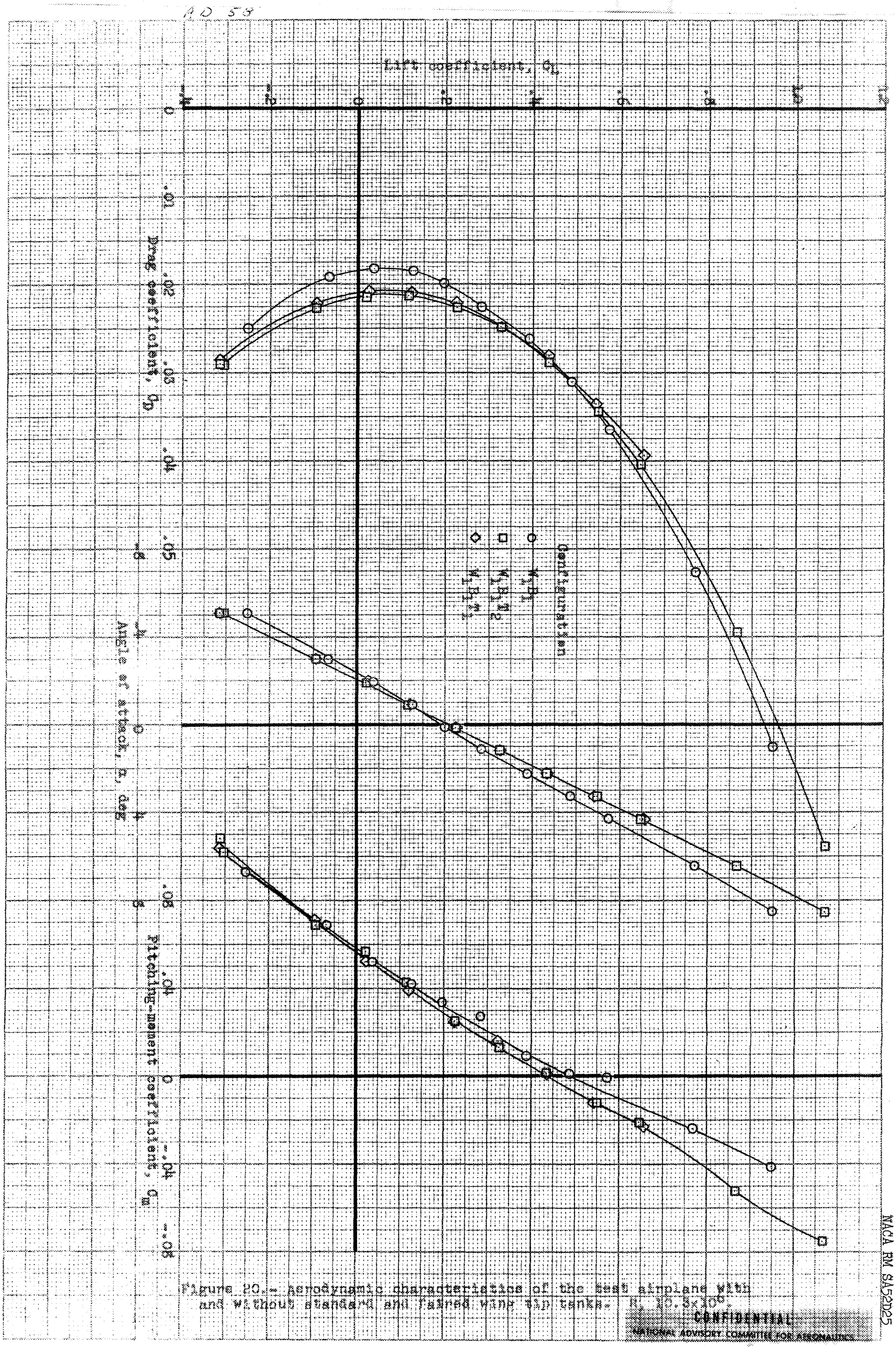

Figure 20.- Aerodynamic characteristics of the basic airplane with and without standard and faired wing tip tanks. R_L 20.3×10^6.

Figure 21.- Effects of several wing changes on the aerodynamic characteristics of the test airplane. R, 10.3×10^6.

(a) C_L vs. C_D.

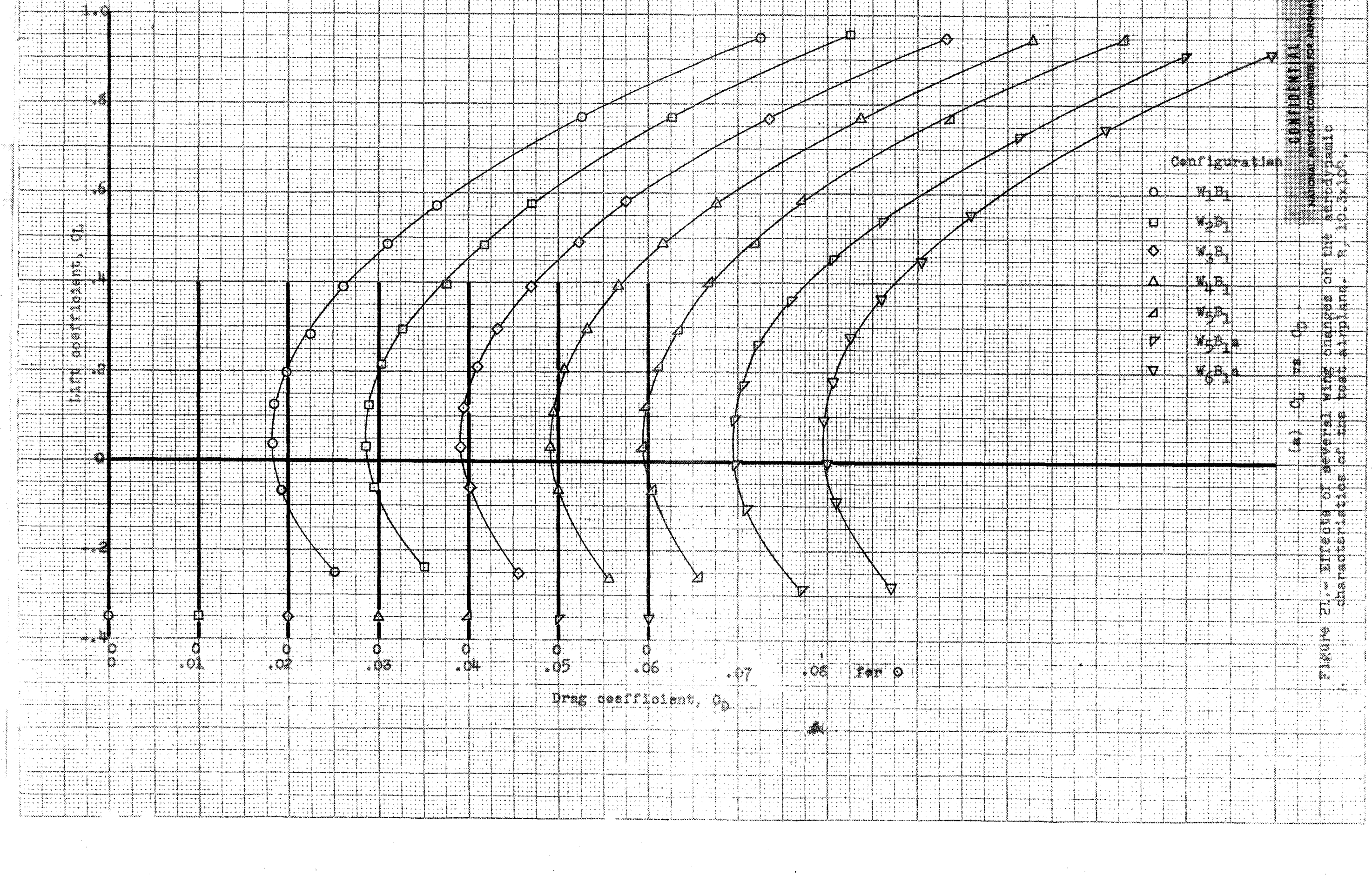

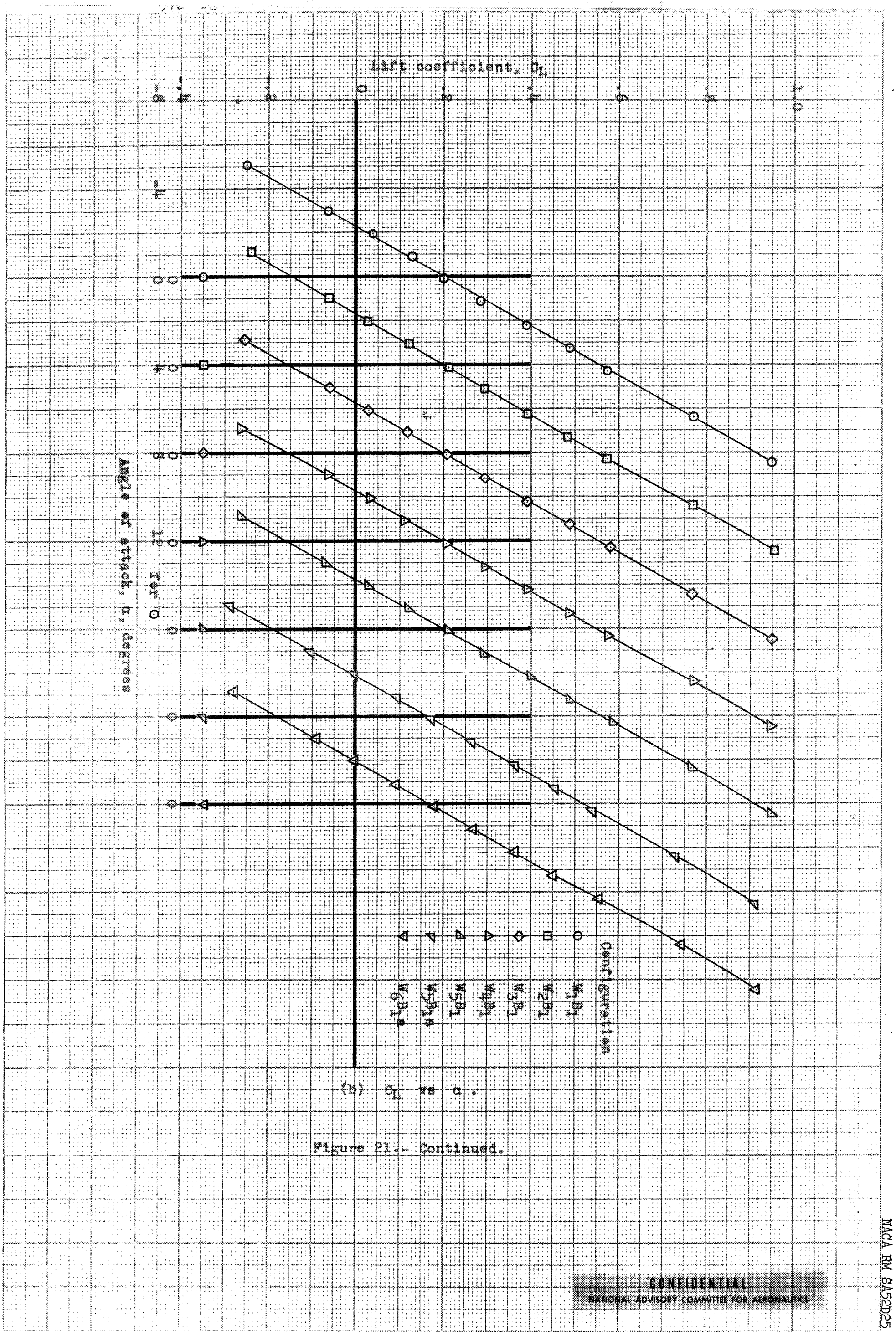

(b) C_L vs α_t.

Figure 21.- Continued.

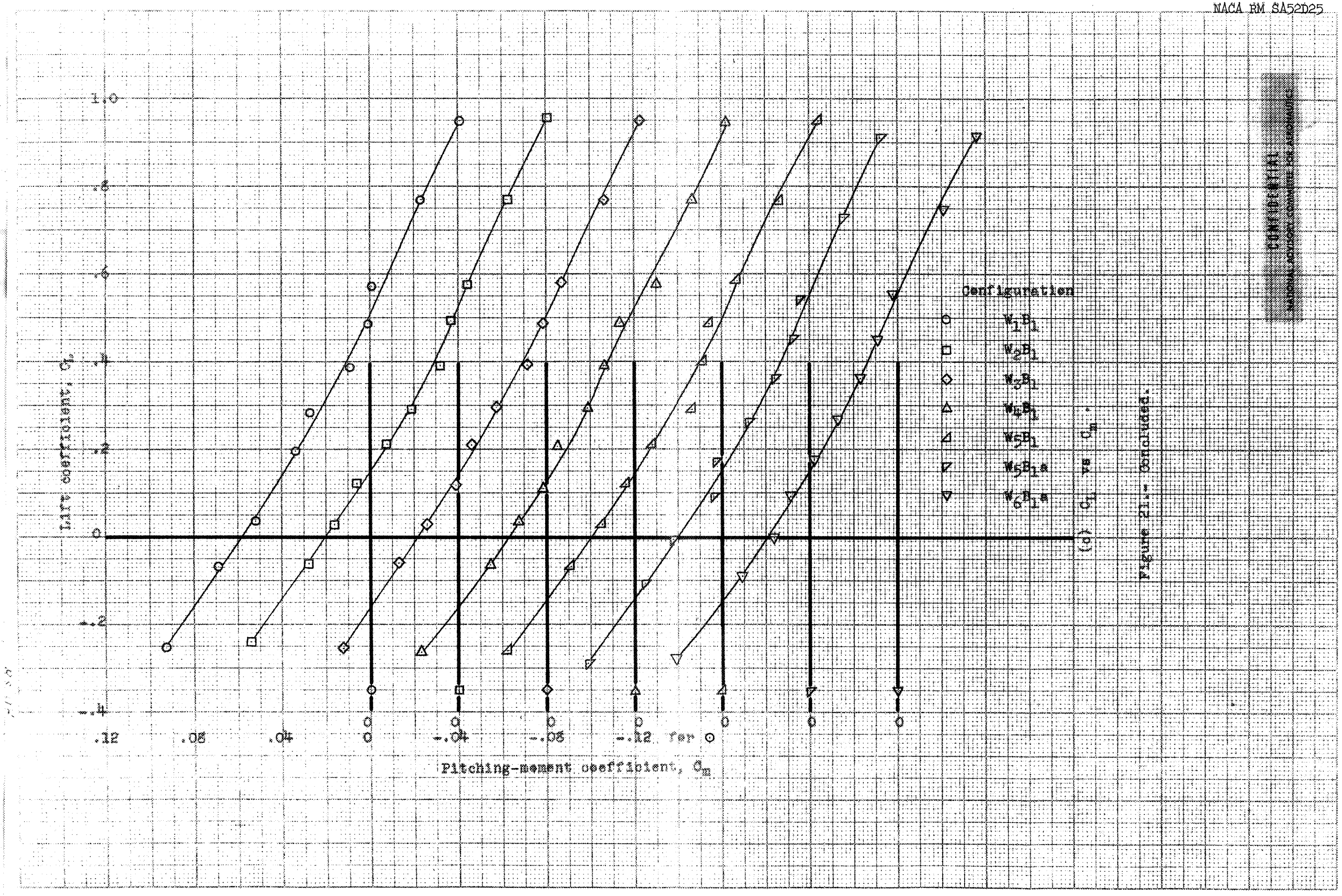

Figure 21.- Concluded.

Figure 22.- Effects of several wing changes on parasite drag of the test airplane. R 10.3x10^6.

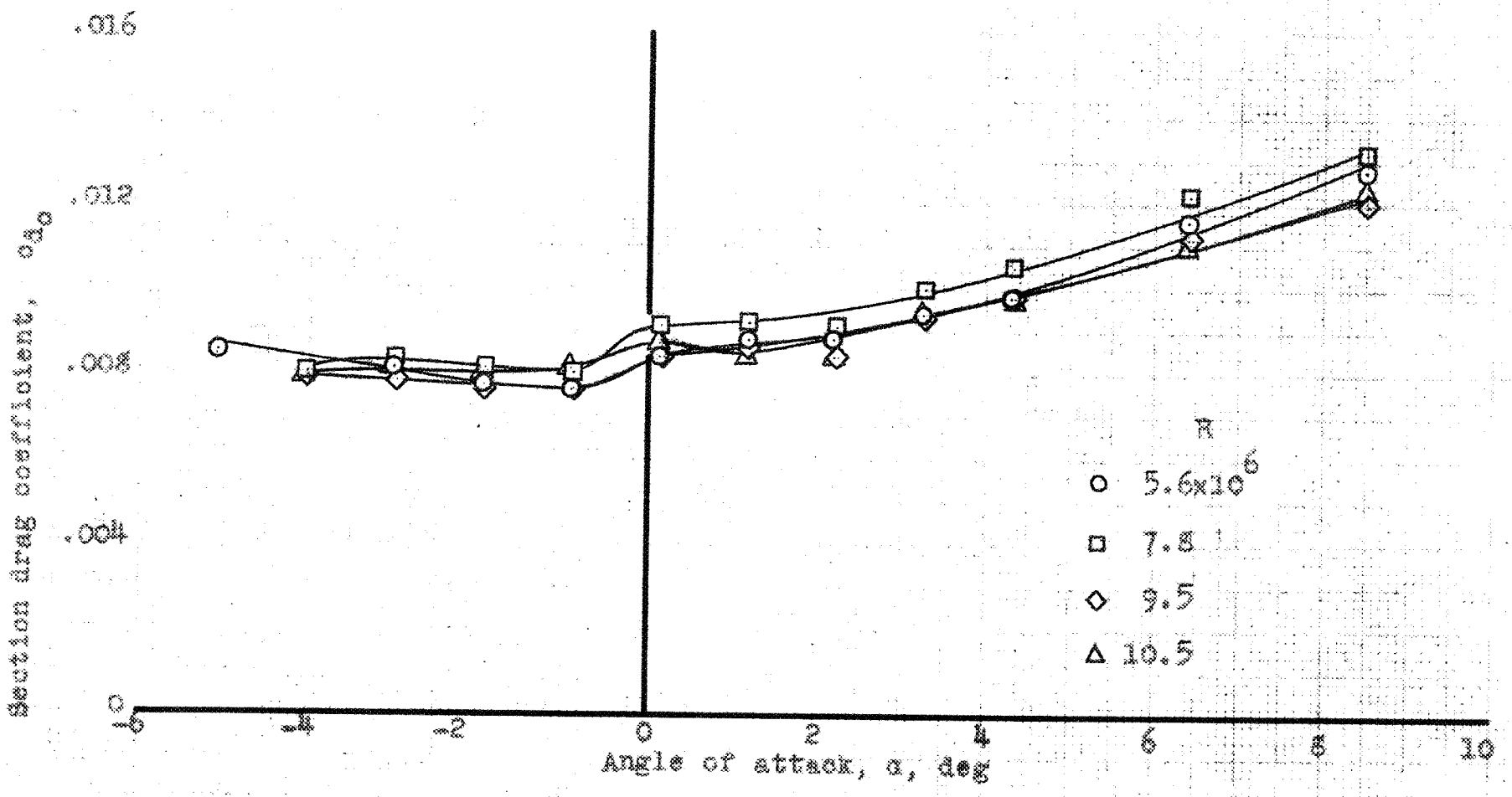

Figure 23.- Wing section drag coefficient at .489 semispan at several Reynolds numbers. Airplane configuration W_1B_1.

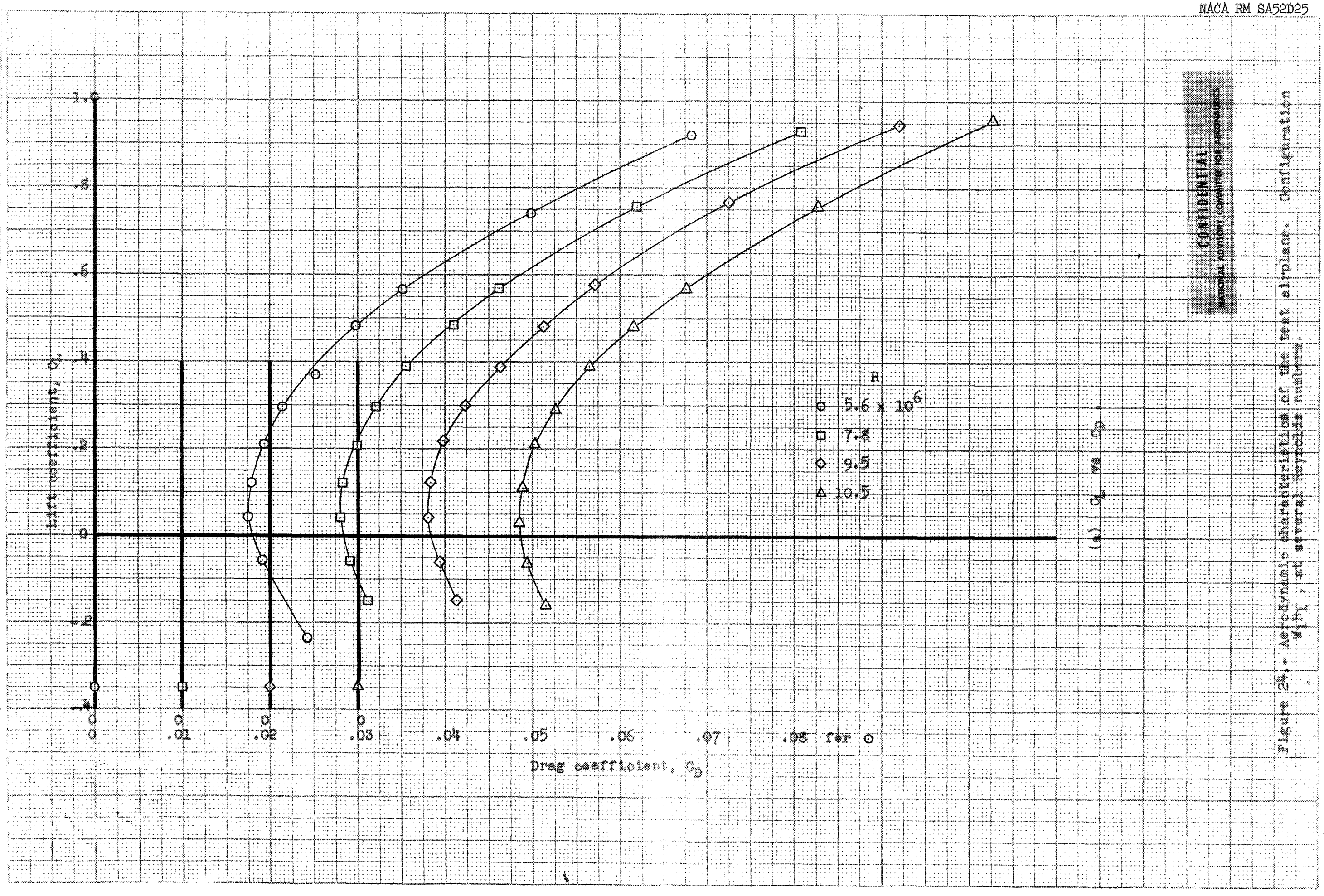

Figure 24.- Aerodynamic characteristics of the test airplane. Configuration with i_t, at several Reynolds numbers.

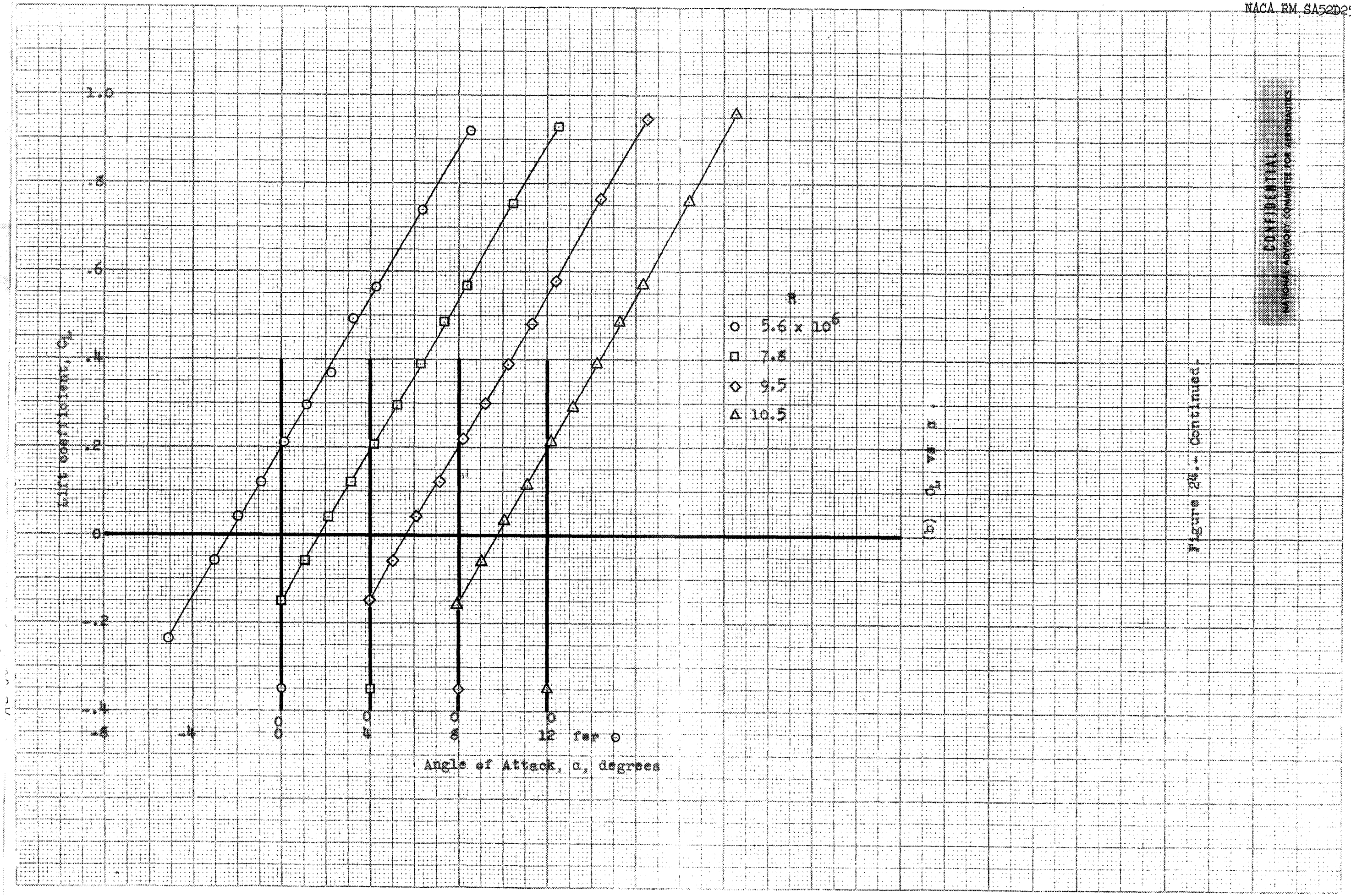

Figure 20.- Continued.

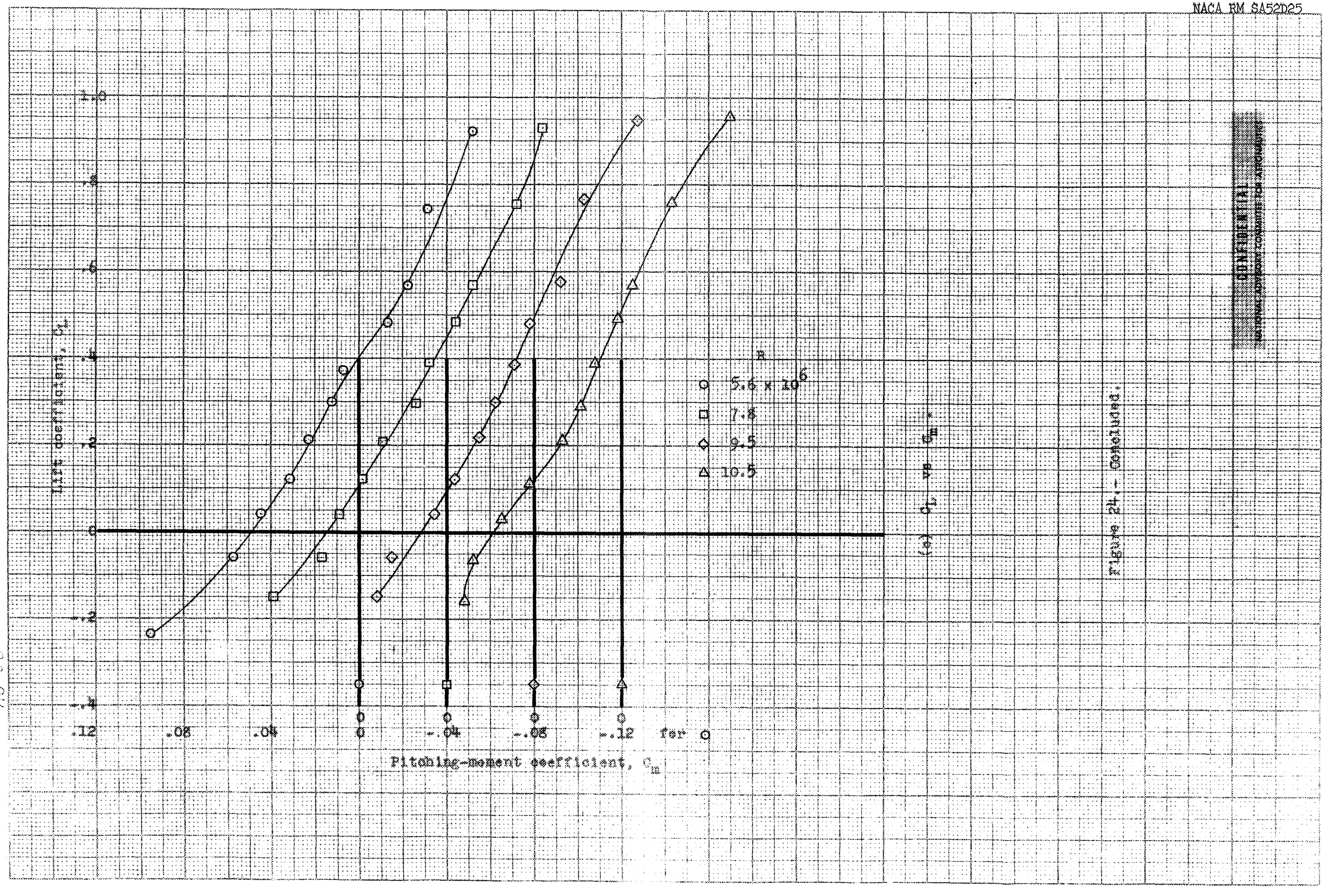

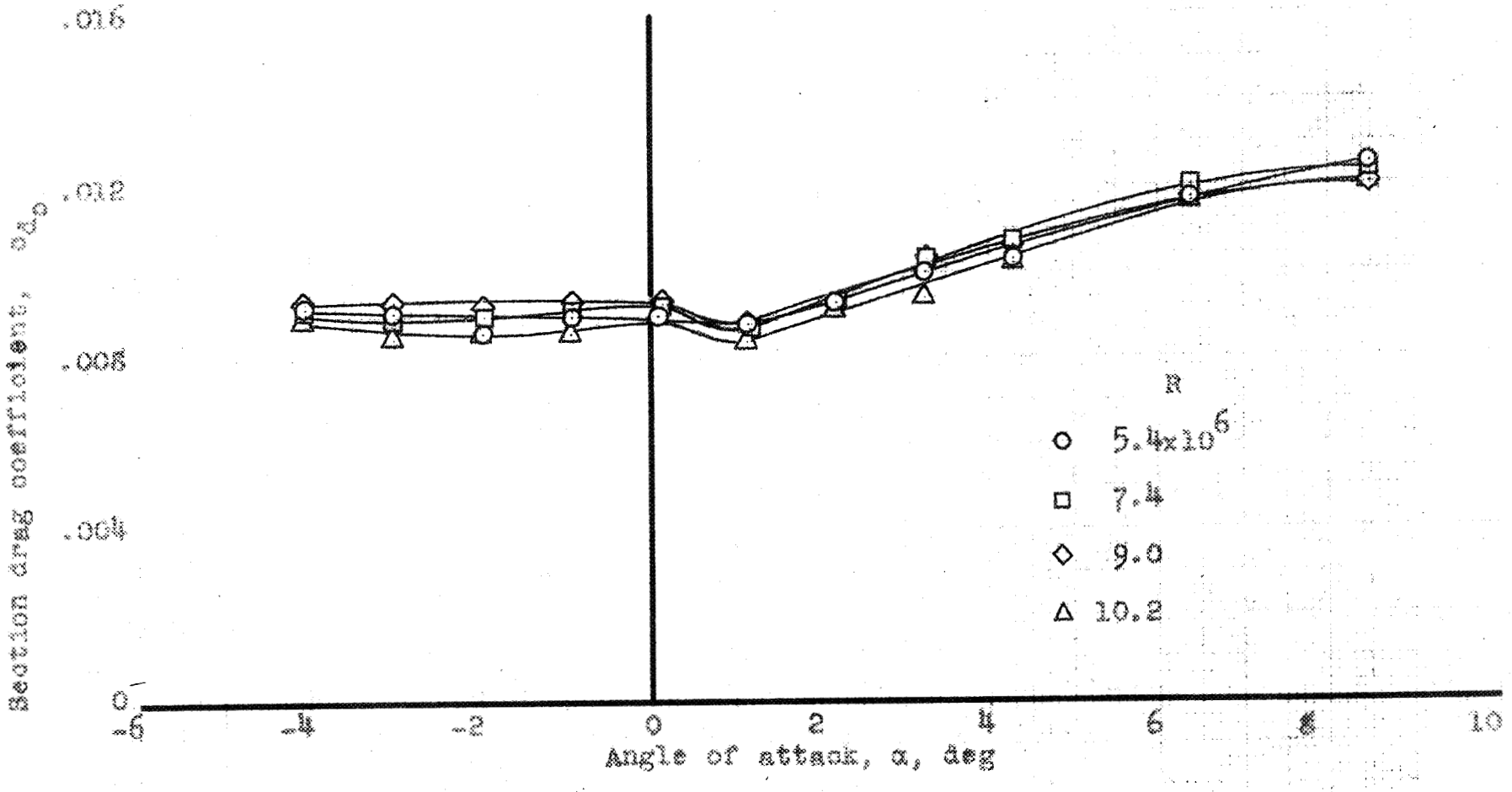

Figure 25.- Wing section drag coefficient at .469 semispan at several Reynolds numbers. Airplane configuration W6B1a.

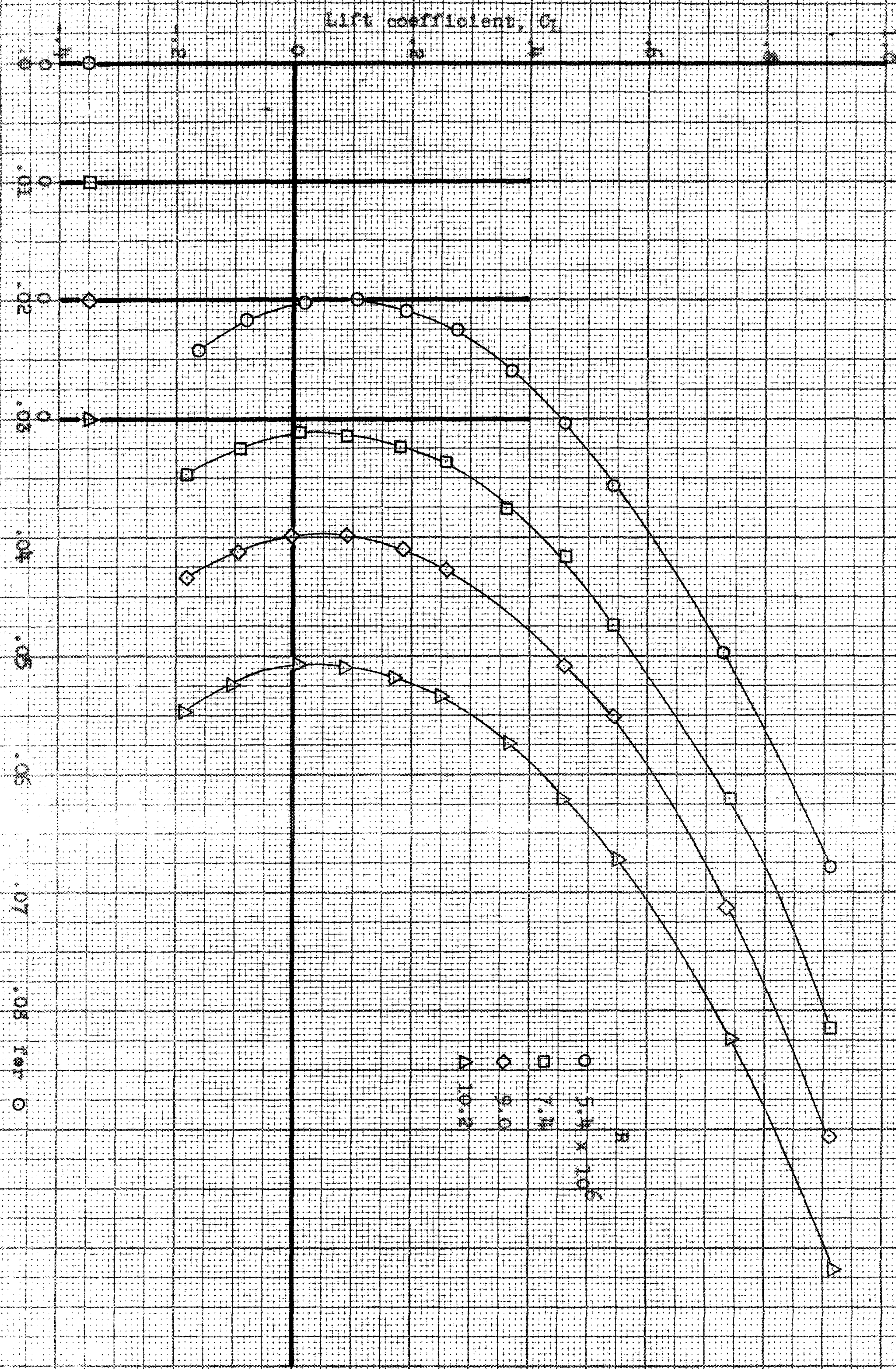

(a) C_L vs C_D.

Figure 26.- Aerodynamic characteristics of the test airplane. Configuration W_5P_1a, at several Reynolds numbers.

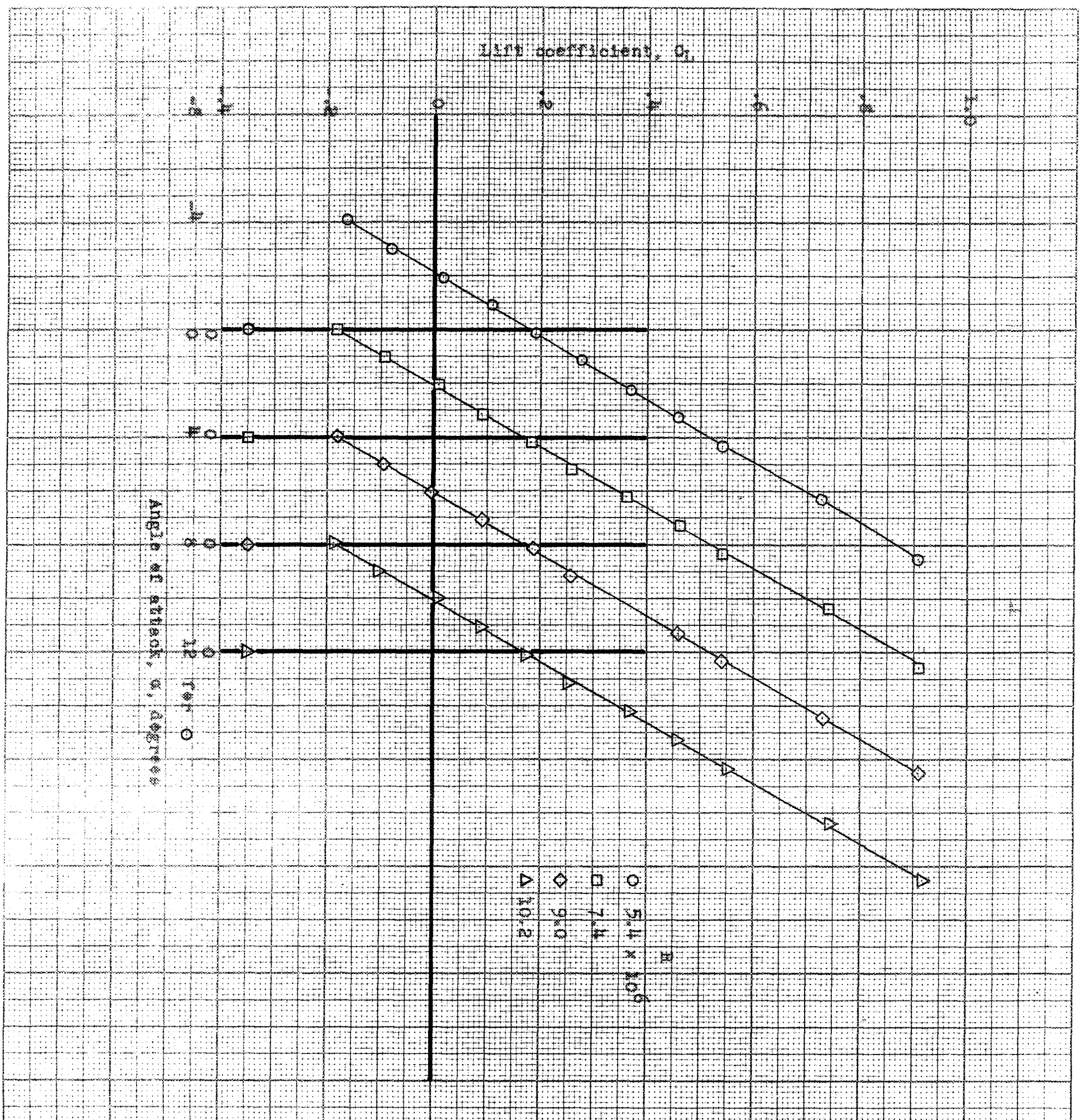

(b) C_L vs α.

Figure 26.- Continued.

Lift coefficient, C_L

1.0
.8
.6
.4
.2
0
-.2
-.4

R
○ 5.4 × 10^6
□ 7.4
◇ 9.0
△ 10.2

.12 .08 .04 0 -.04 -.08 -.12 for ○

Pitching-moment coefficient, C_m

(a) $C_{m_{cg}}$ vs. C_L.

Figure 25.- Concluded.

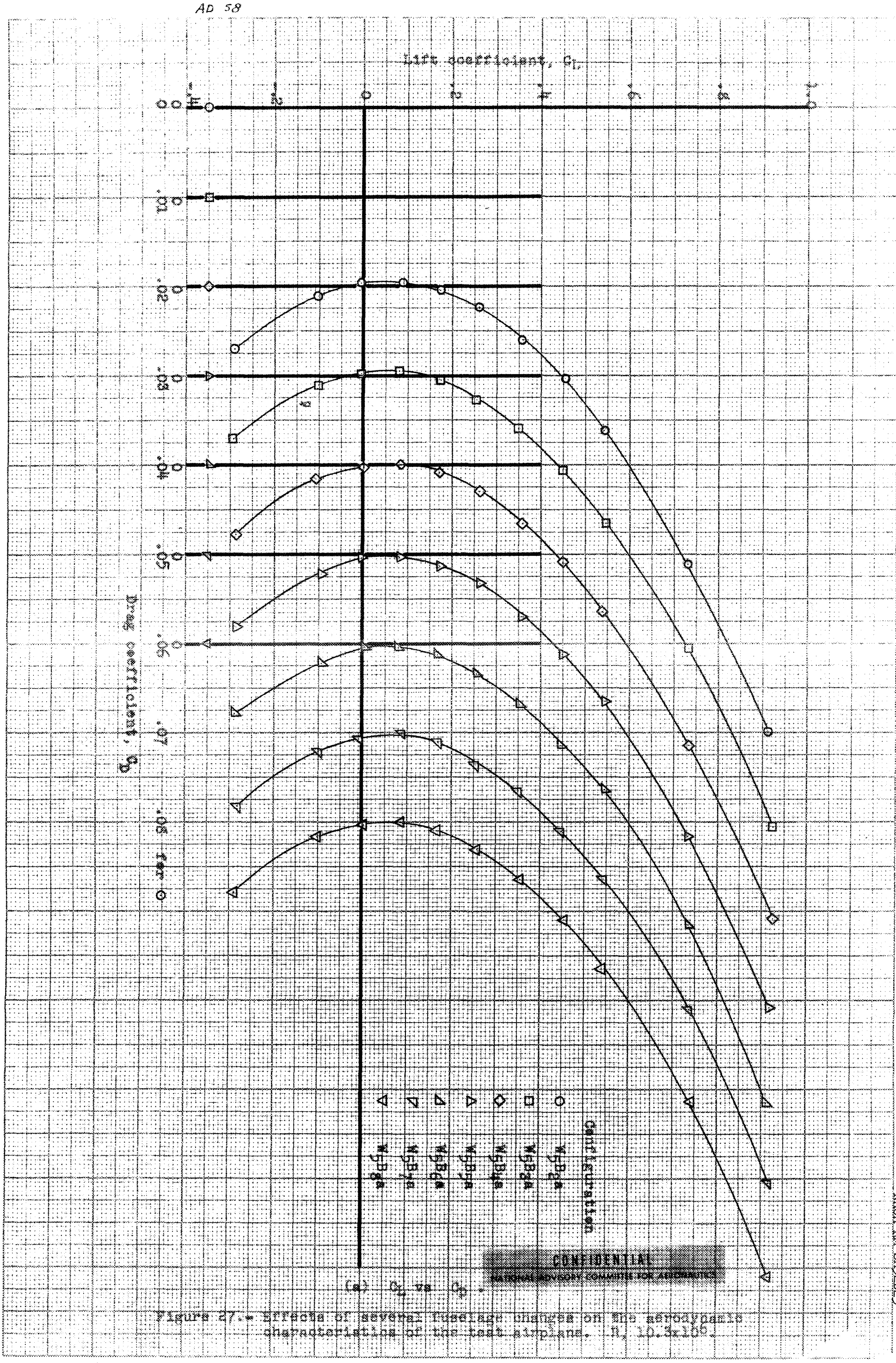

Figure 27.- Effects of several fuselage changes on the aerodynamic characteristics of the test airplane. R_L 10.3x10^6.

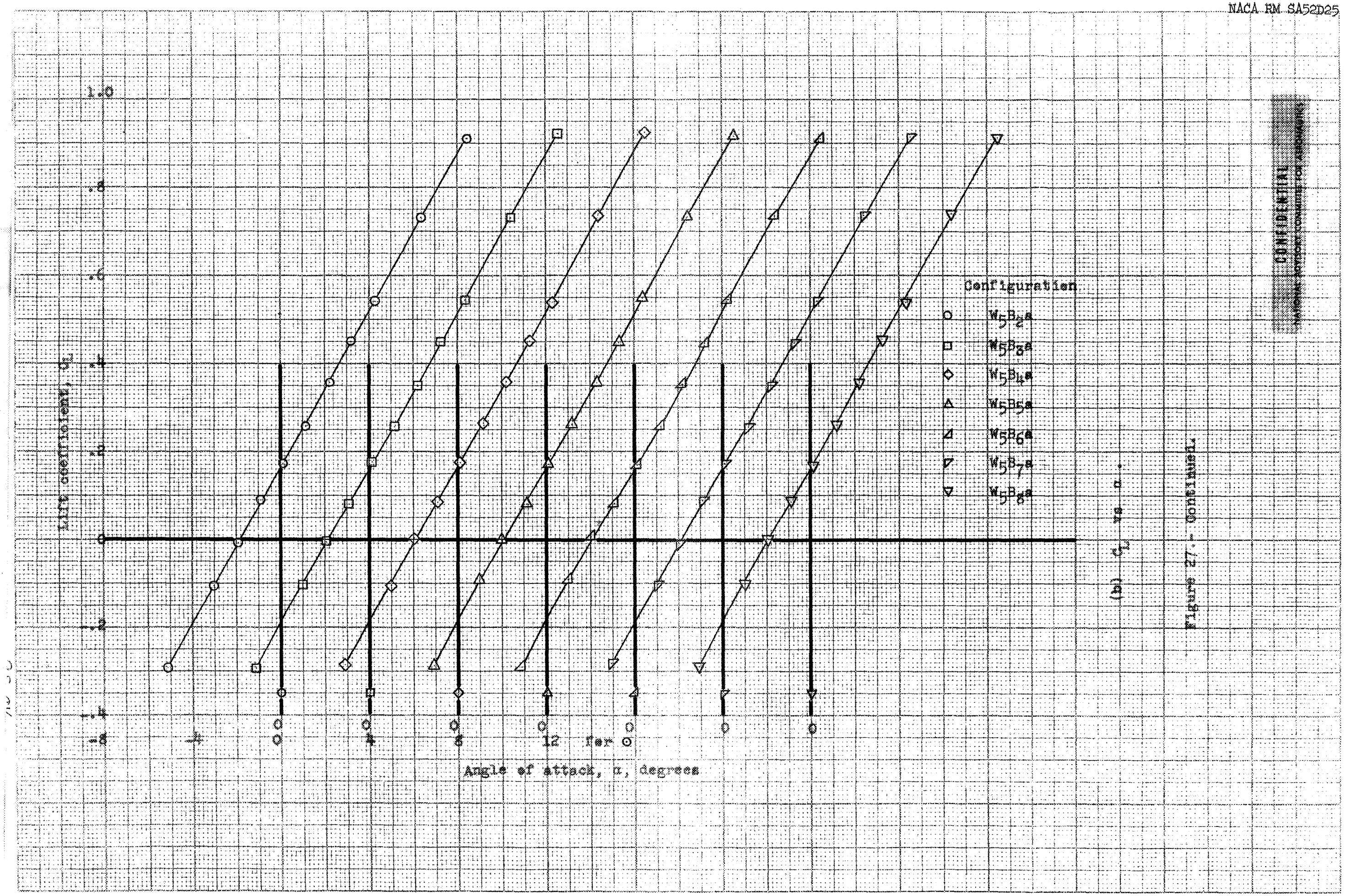

(b) C_L vs α

Figure 27.- Continued

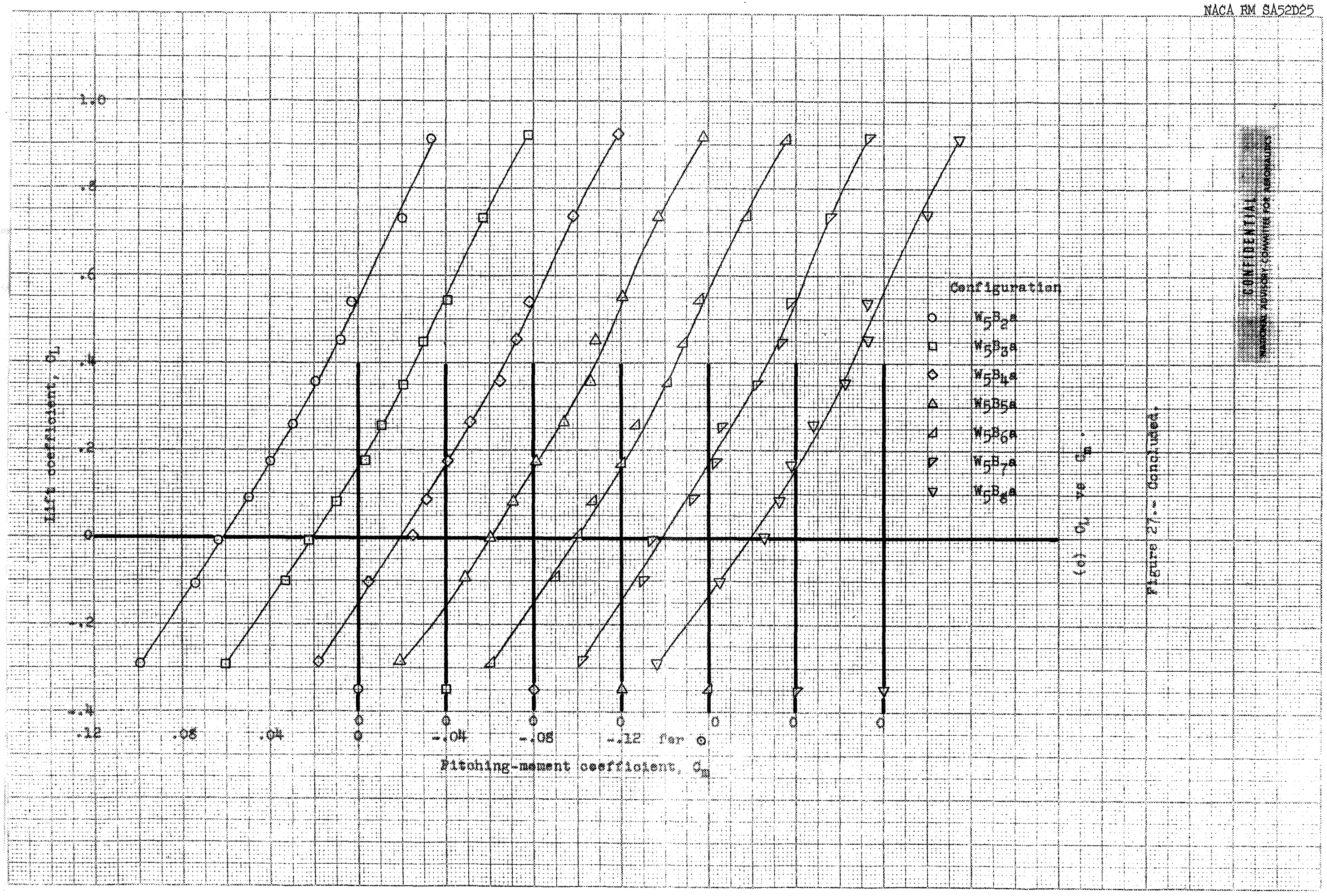

Figure 27.- Concluded.

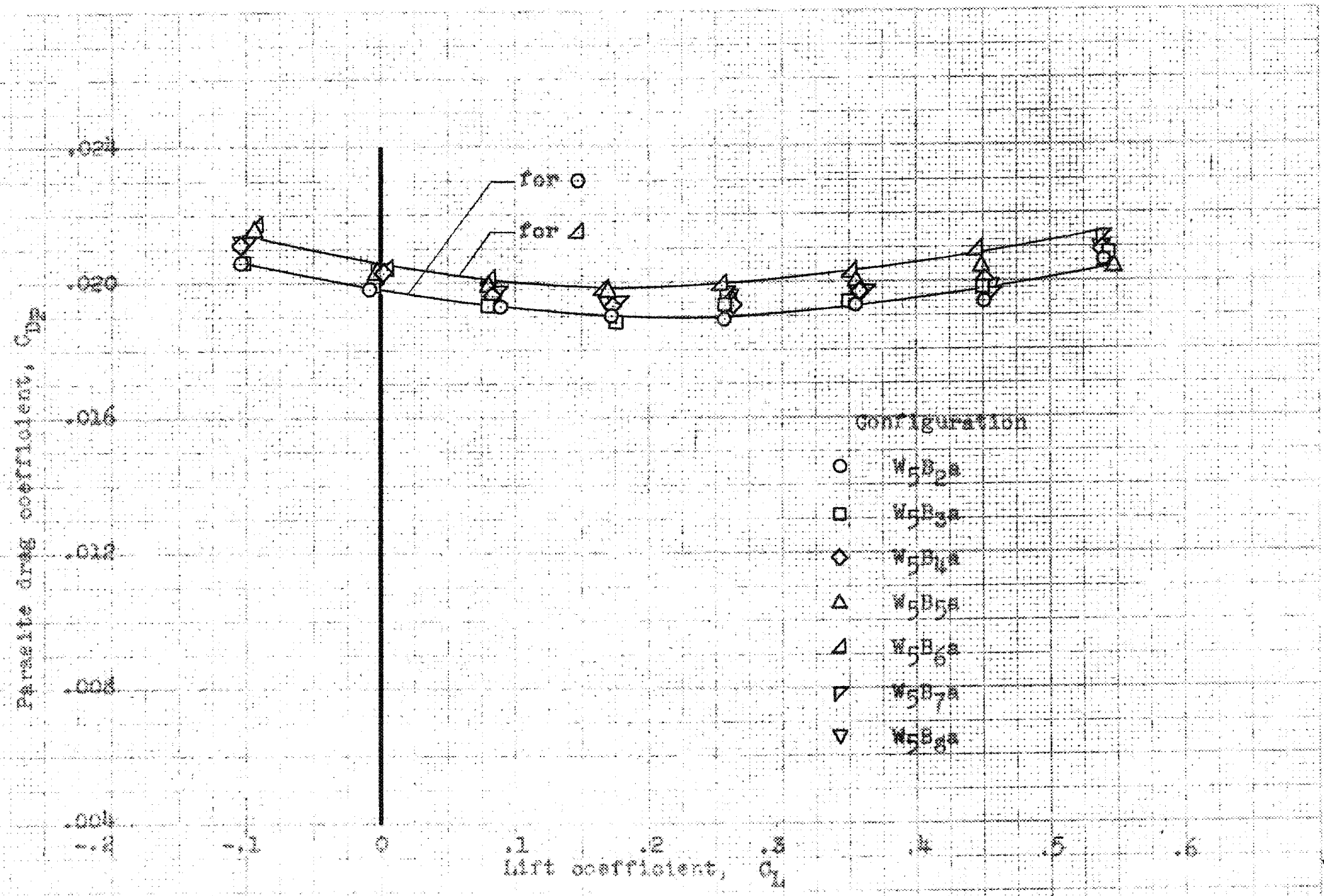

Figure 25.- Effects of several fuselage changes on the parasite drag of the test airplane. R, 10.3×10^6.

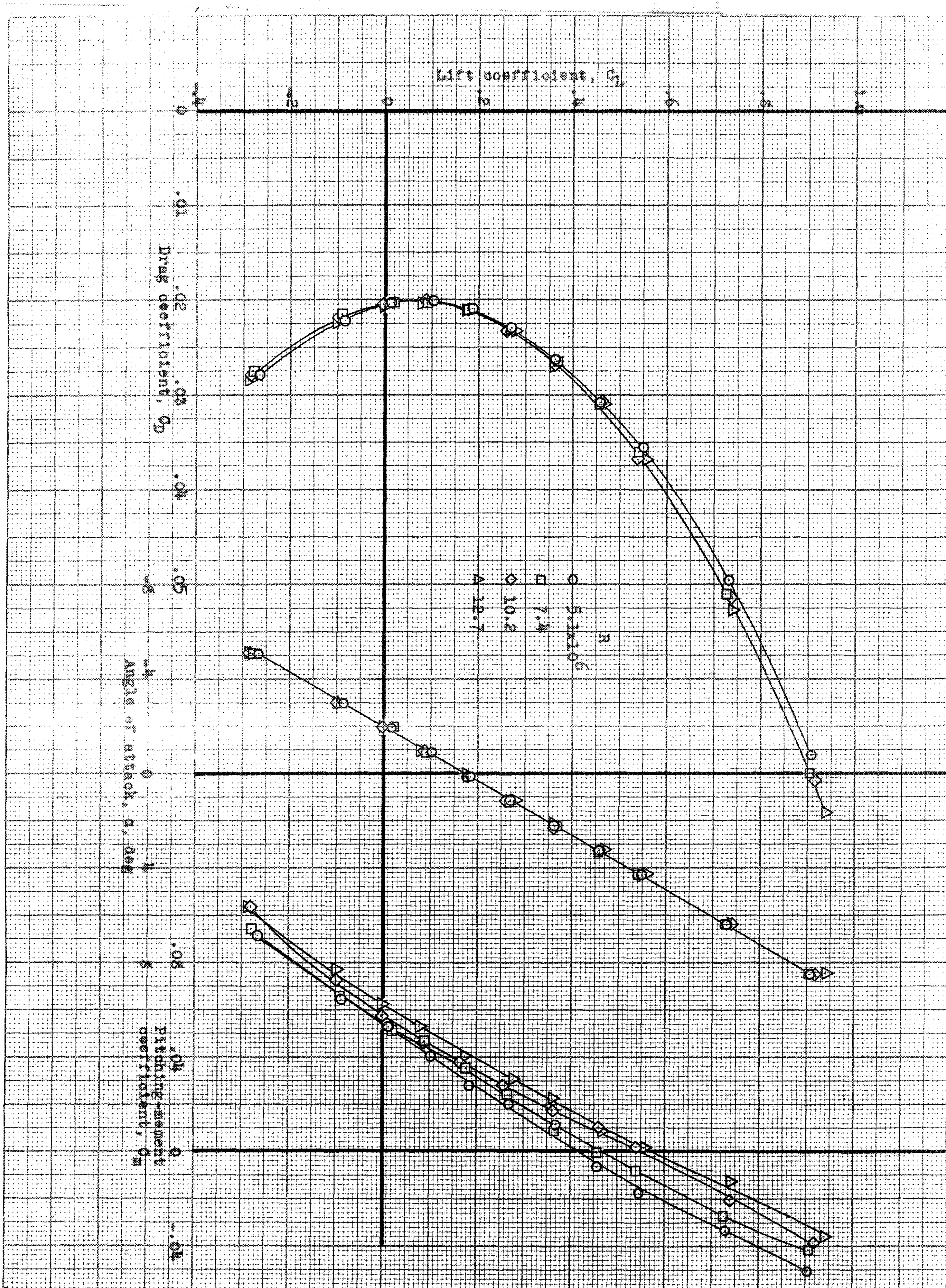

Figure 29.- Aerodynamic characteristics of the test airplane. Configuration W_5B_7s , at several Reynolds numbers.

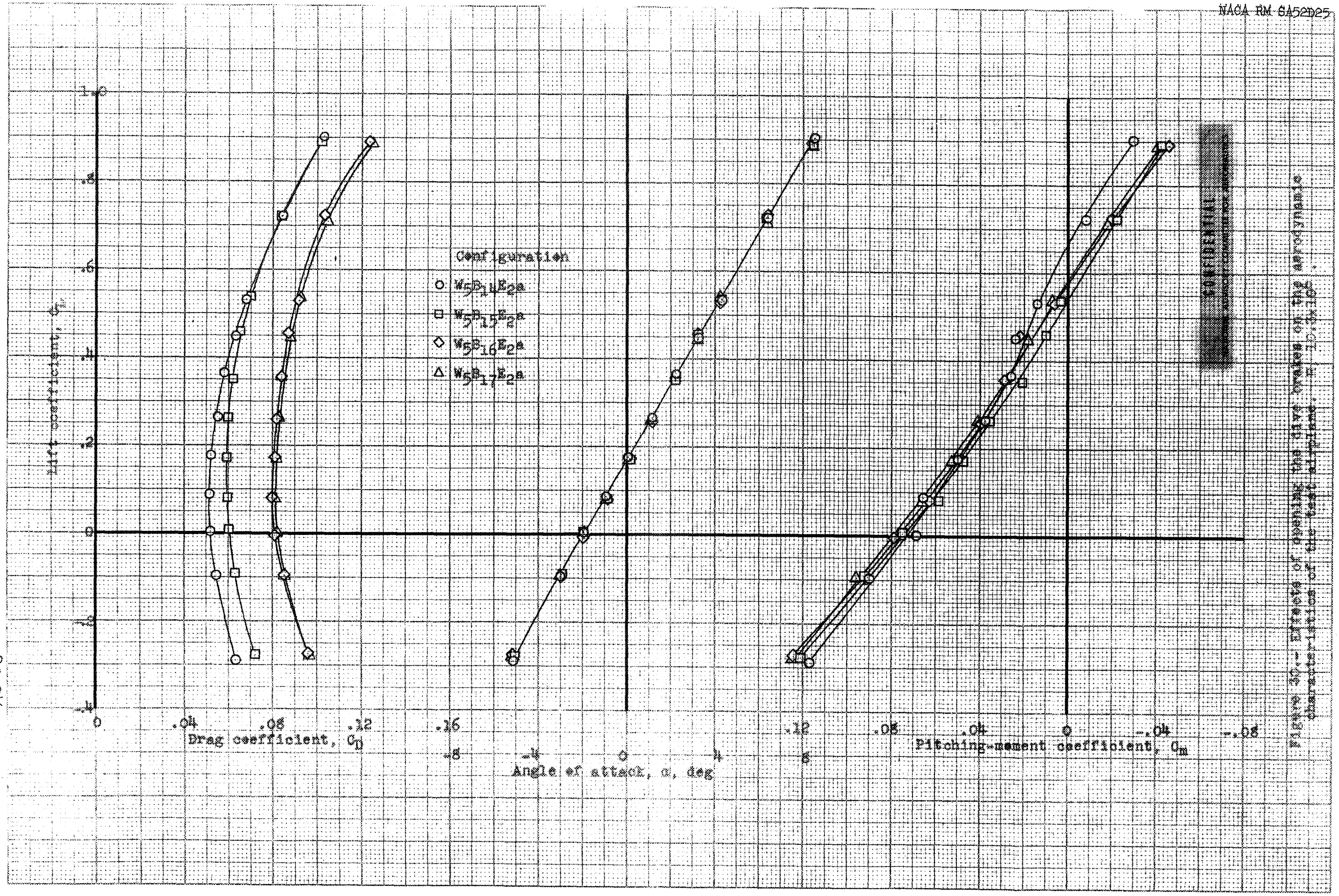

Figure 30.- Effects of deploying the data windows on the aerodynamic characteristics of the test configuration.

A0 58

Figure 31.- Effects of opening the dive brakes on the parasite drag of the test airplane. R, 10.3×10^6.

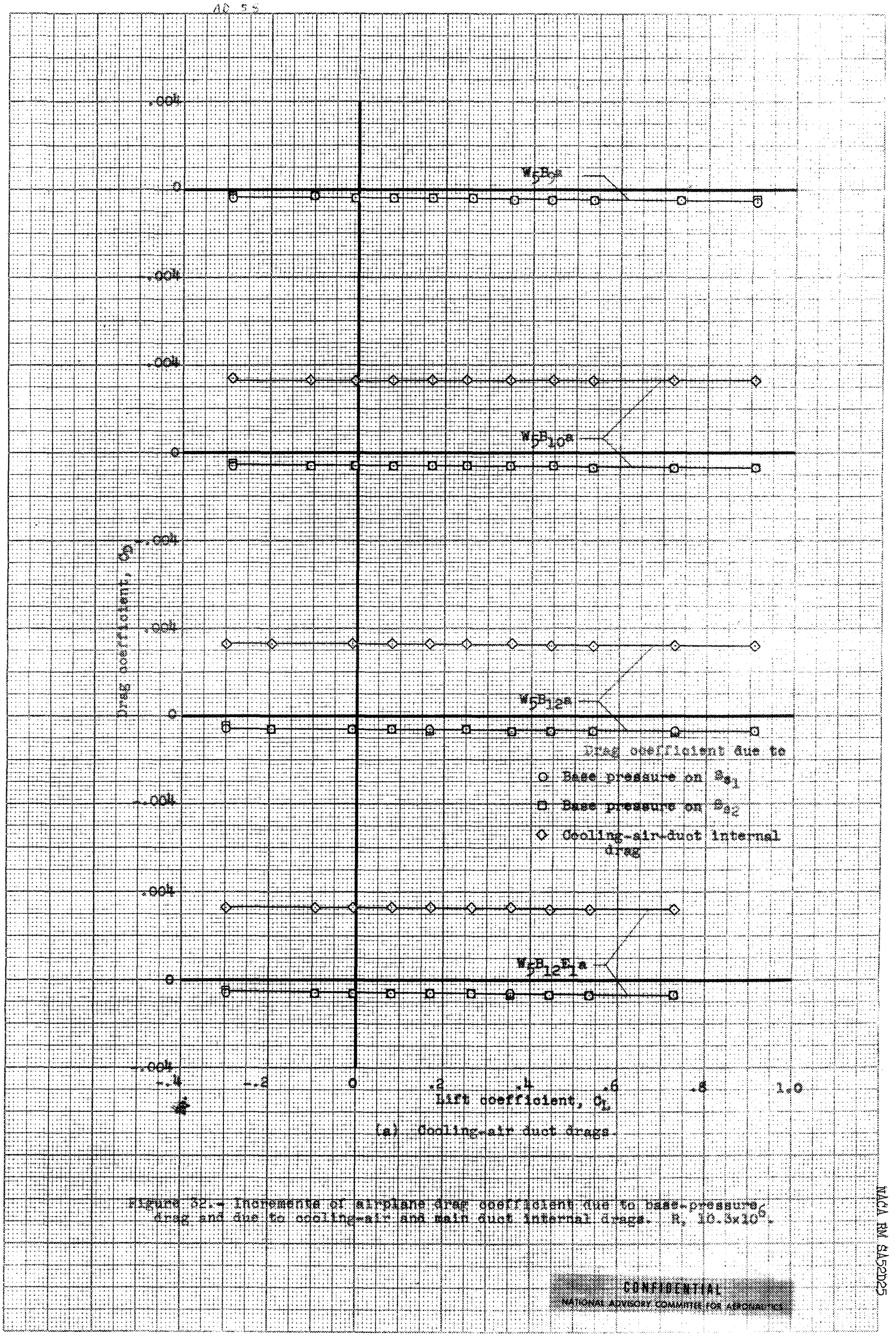

(a) Cooling-air duct drags.

Figure 52.- Increments of airplane drag coefficient due to base-pressure drag and due to cooling-air and main duct internal drags. R, 10.3×10^6.

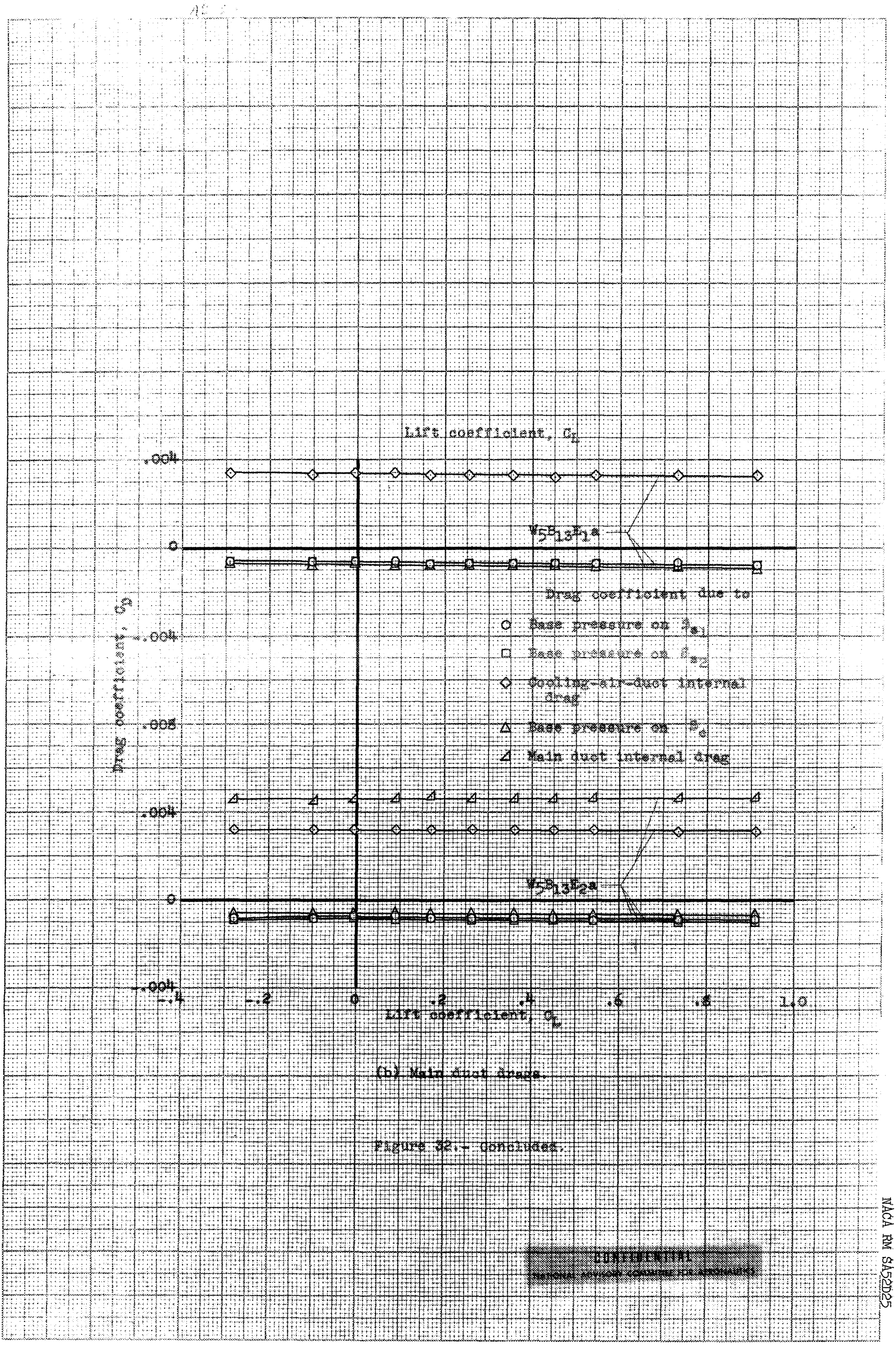

(b) Main duct drags.

Figure 32.- Concluded.

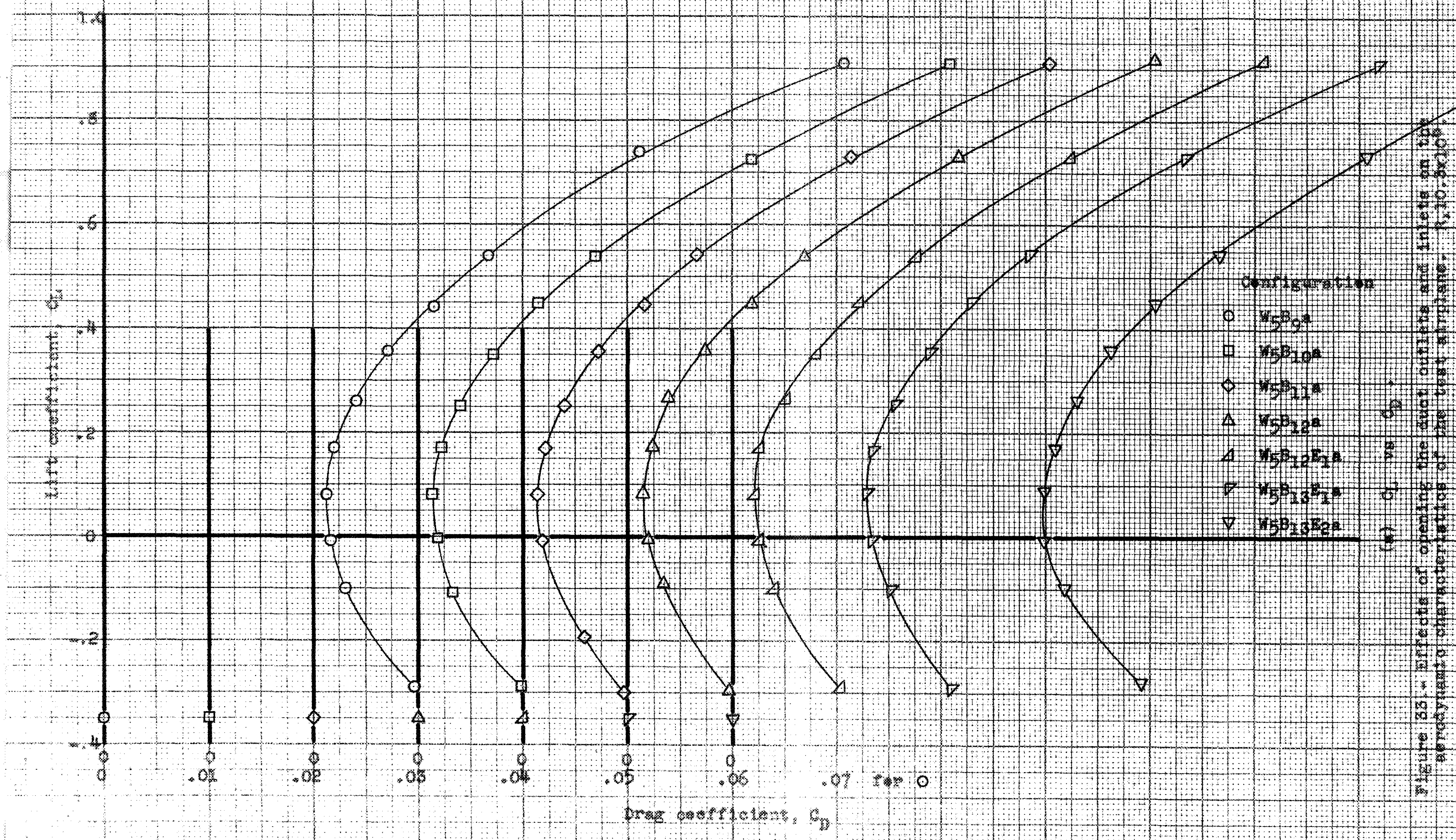

(a) C_L vs C_D.

Figure 33.- Effects of opening the duct outlets and inlets on the aerodynamic characteristics of the test airplane. R, 10.3×10^6.

AD 58

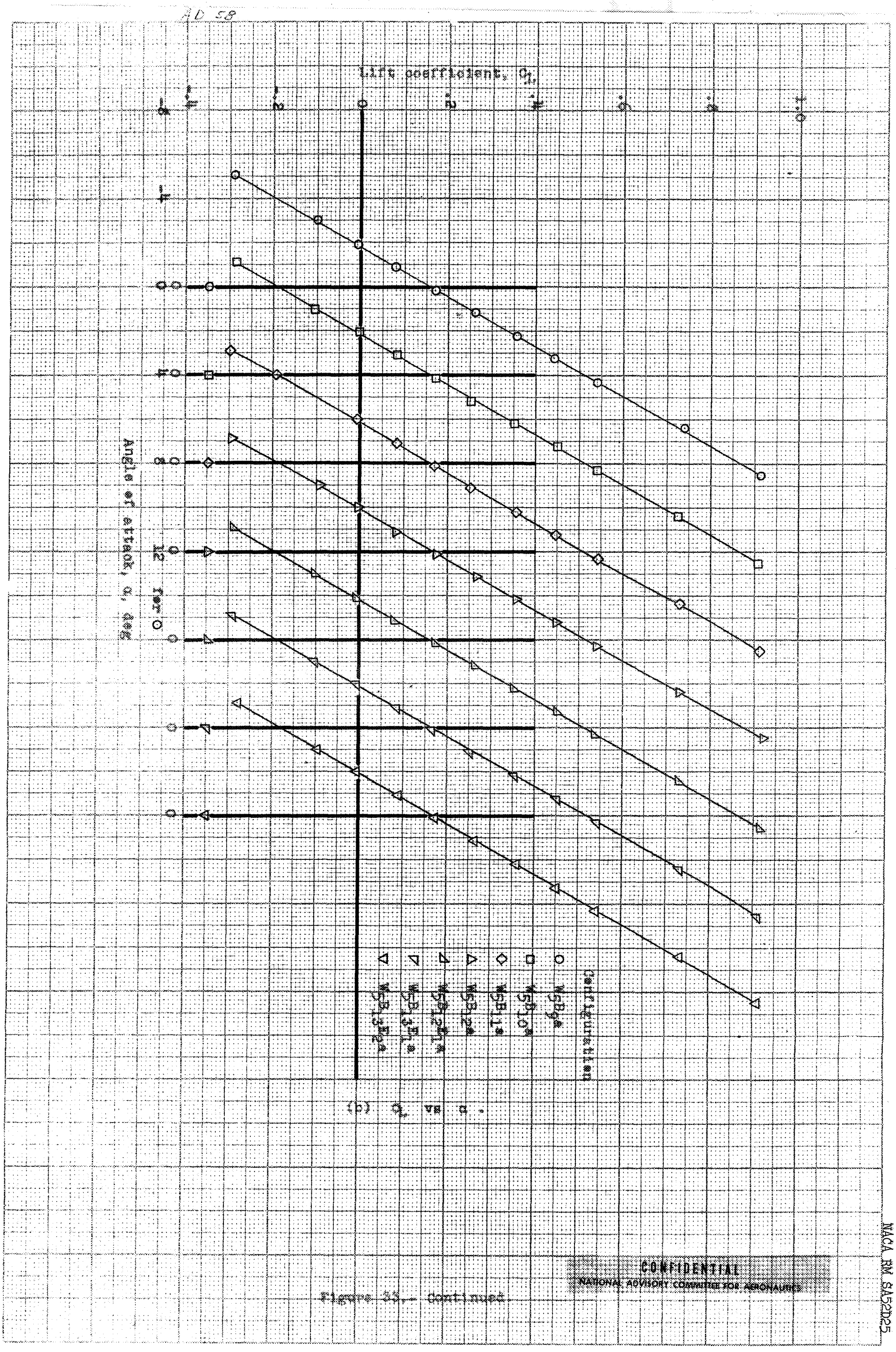

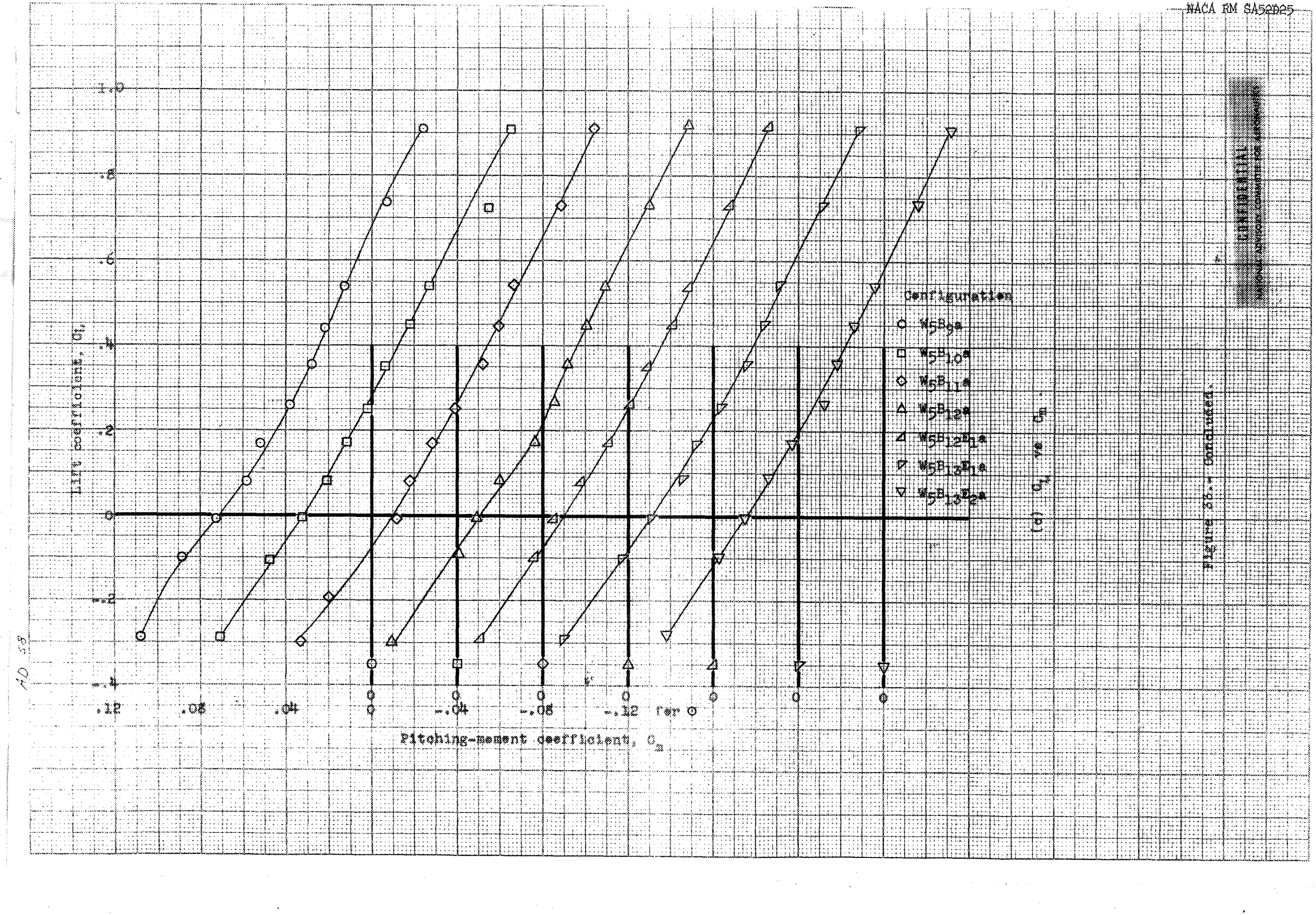

Figure 35.- Concluded.

AD 58

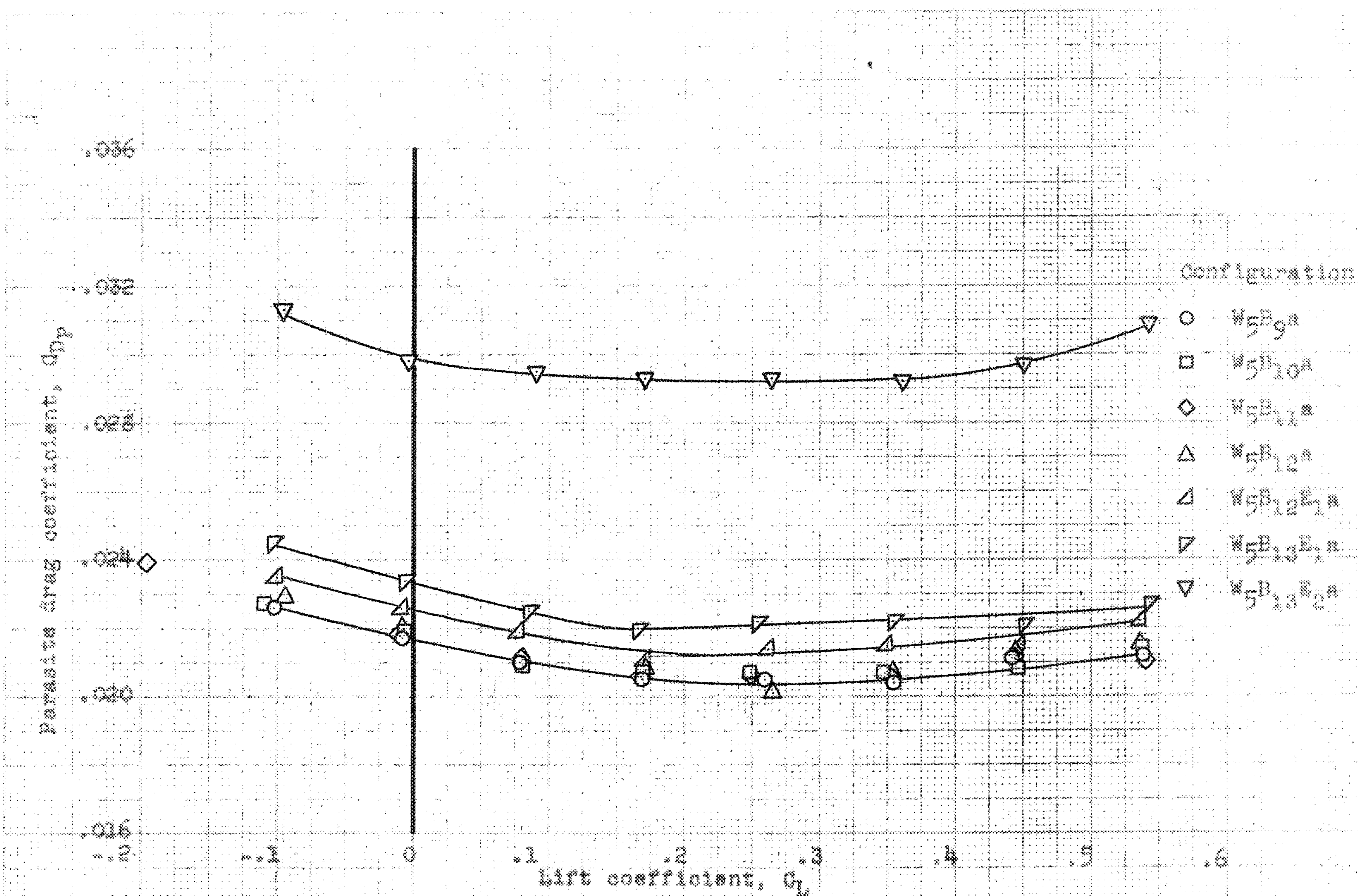

Figure 34.- Effects of opening the duct outlets and inlets on the parasite drag of the test airplane. R, 10.3×10^6.

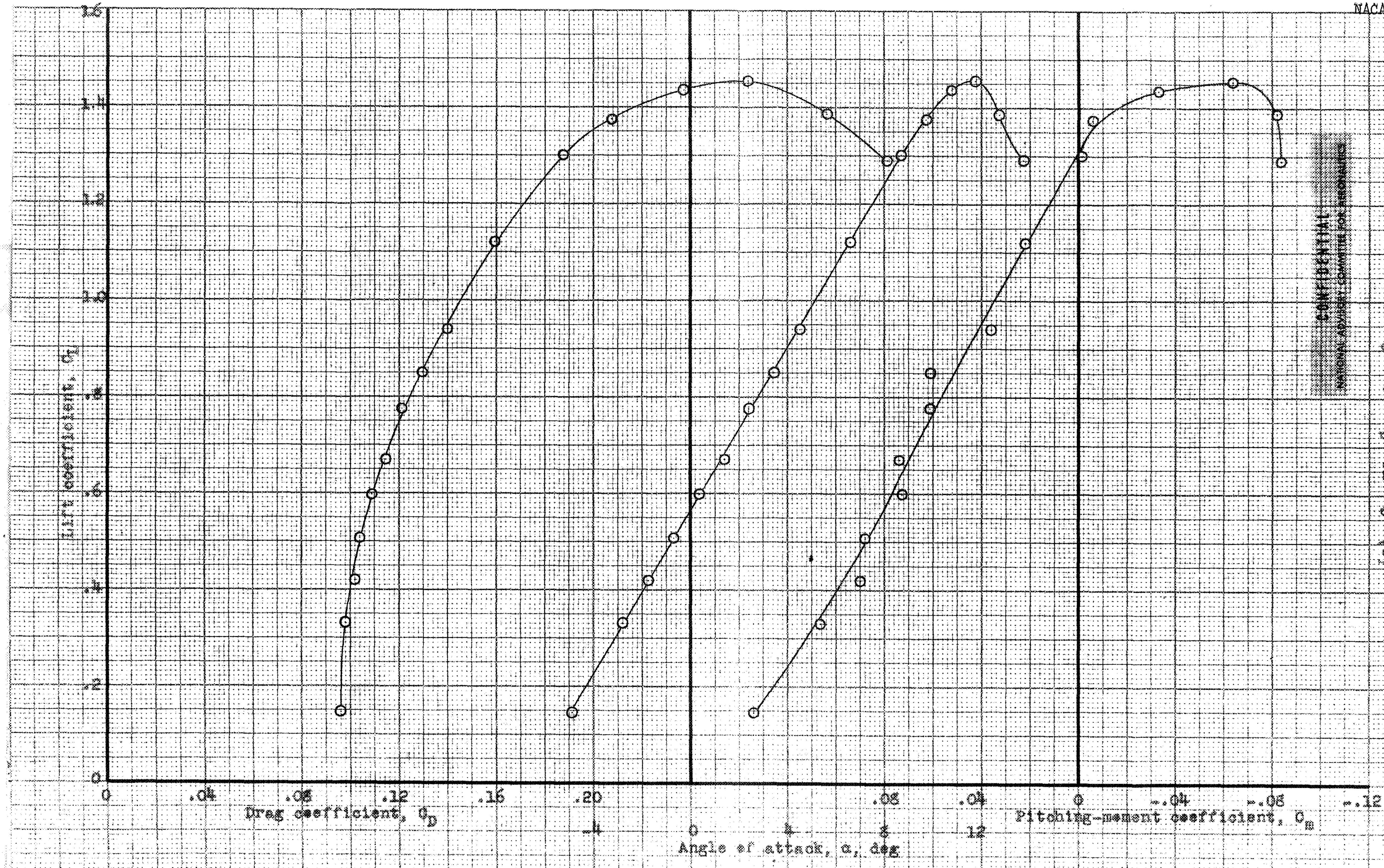

(a) C_L vs C_D , α , C_m .

Figure 35.- Aerodynamic characteristics of the test airplane. Configuration $W_5H_{13}E_2ac$. R, 7.8×10^6 .

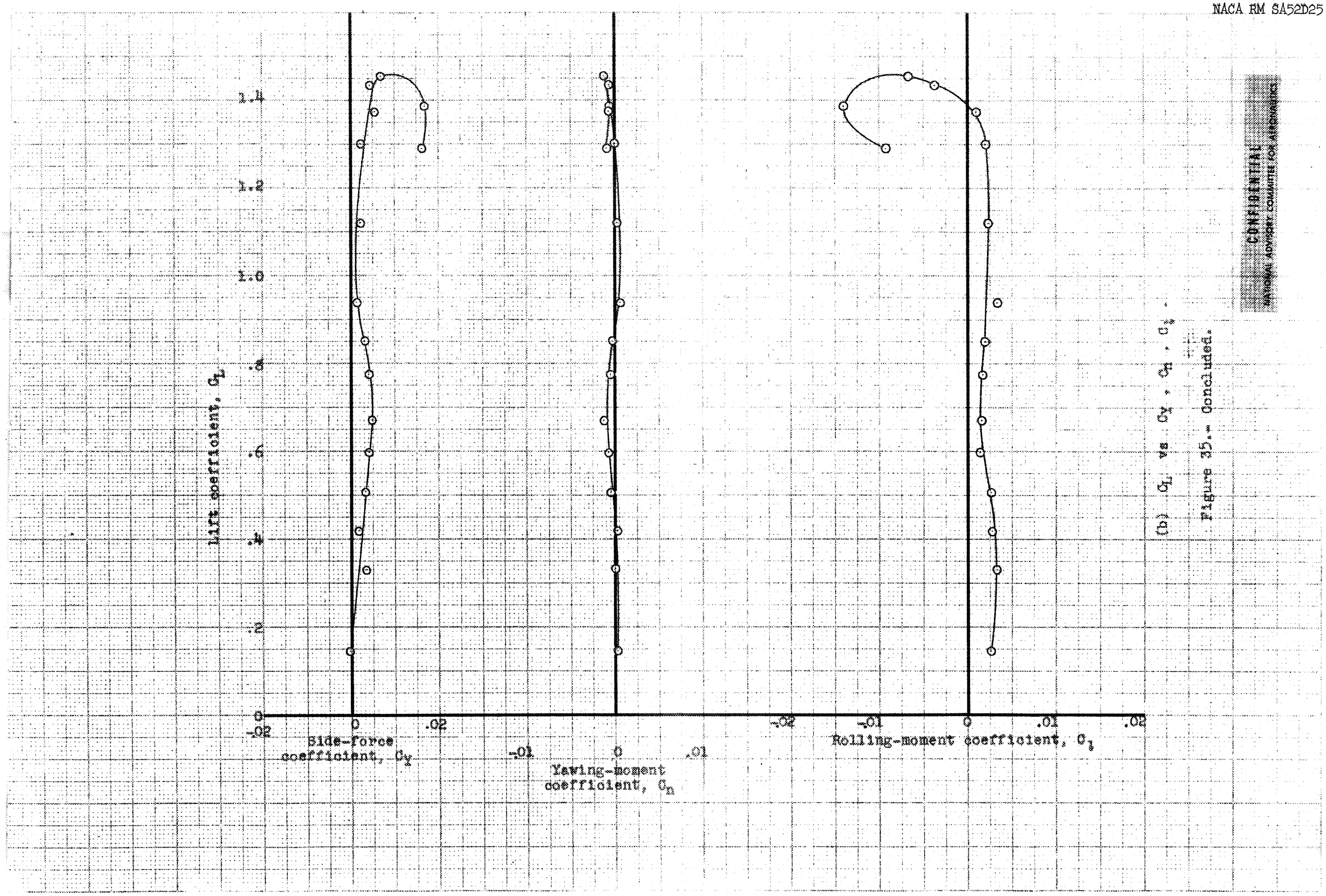

(b) C_L vs C_Y, C_n, C_l.

Figure 35.- Concluded.

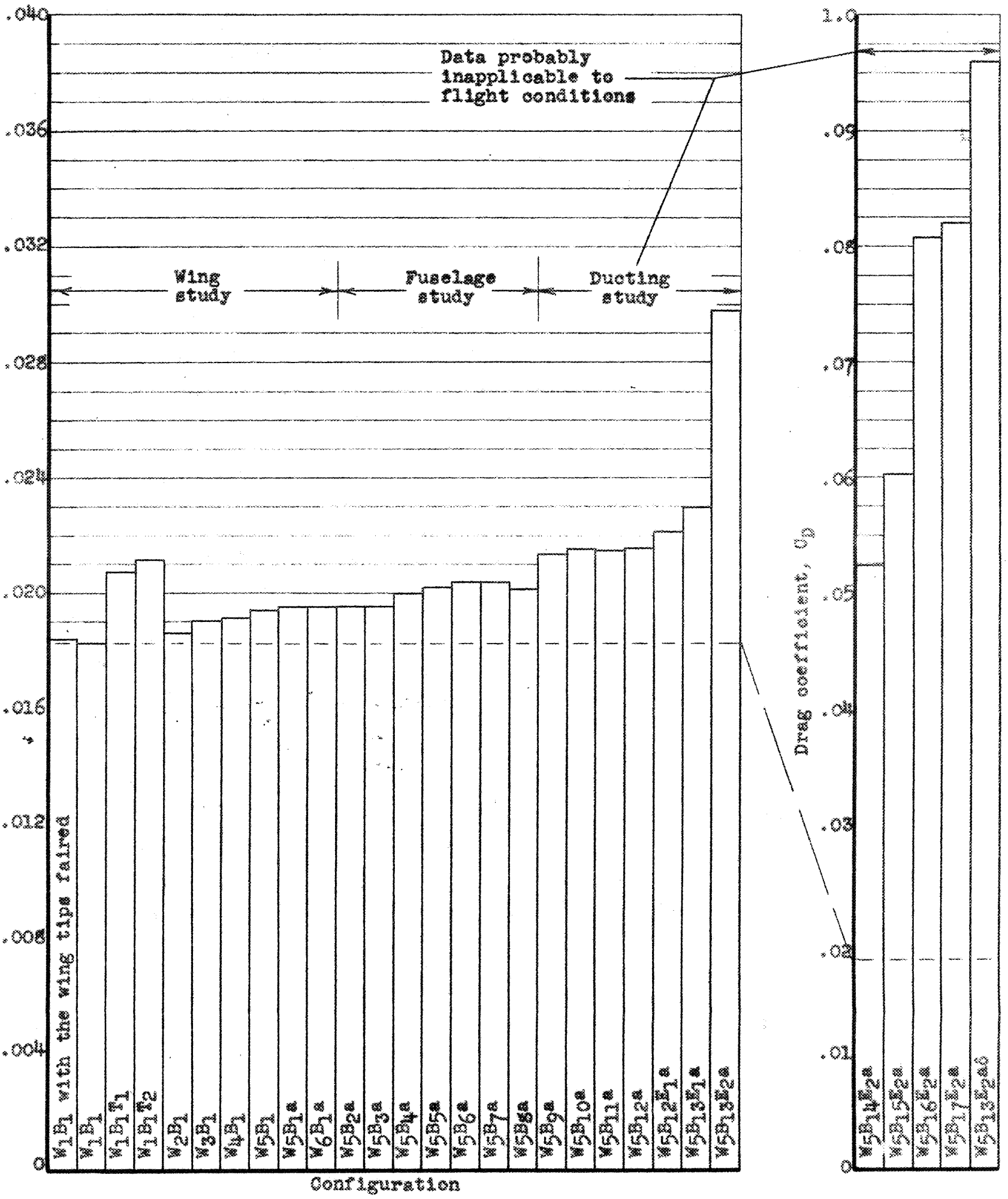

Figure 36.- Summary of the minimum drag coefficients at a Reynolds number of 10.3×10^6.